Deep–Sea Research I 172 (2021) 103533

Contents lists available at ScienceDirect

Deep-Sea Research Part I

journal homepage: http://www.elsevier.com/locate/dsri

A view of the Brazil-Malvinas confluence, March 2015

Dorleta Orúe-Echevarría [a,*], Josep L. Pelegrí [a,**], Iván J. Alonso-González [b], Verónica M. Benítez-Barrios [b], Mikhail Emelianov [a], Antonio García-Olivares [a], Marc Gasser i Rubinat [a], Patricia De La Fuente [a], Carmen Herrero [a], Jordi Isern-Fontanet [a], Marta Masdeu-Navarro [a], Jesús Peña-Izquierdo [a], Alberto R. Piola [c,d,e], Sergio Ramírez-Garrido [a], Miquel Rosell-Fieschi [a], Joaquín Salvador [a], Martín Saraceno [c,e,f,g], Daniel Valla [c,d], Ignasi Vallès-Casanova [a], Montserrat Vidal [g]

[a] Departament d'Oceanografia Física i Tecnològica, Institut de Ciències del Mar, ICM-CSIC, Unidad Asociada ULPGC-CSIC, Barcelona, Spain
[b] OCEOMIC, Marine Bio and Technology S.L., Fuerteventura Technology Park, Puerto del Rosario, Spain
[c] Centro de Investigaciones del Mar y la Atmósfera, CIMA-CONICET/UBA, Buenos Aires, Argentina
[d] Departamento de Oceanografía, Servicio de Hidrografía Naval, DCAO/FCEN/UBA, Buenos Aires, Argentina
[e] Departamento de Ciencias de la Atmósfera y de los Océanos, FCEN, Universidad de Buenos Aires, Buenos Aires, Argentina
[f] Unidad Mixta Internacional-Instituto Franco-Argentino para el Estudio del Clima y sus Impactos (UMI-IFAECI-CONICET-UBA-IRD), Buenos Aires, Argentina
[g] Departament de Biologia Evolutiva, Ecologia i Ciències Ambientals, Universitat de Barcelona, Barcelona, Spain

ARTICLE INFO

Keywords:
Brazil-Malvinas Confluence
Ocean currents
River plume
Ageostrophic velocity
Lagrangian description
Hydrographic data

ABSTRACT

The encountering of the subtropical Brazil Current (BC) and the subantarctic Malvinas Current (MC) along the western margin of the Argentine Basin forms the Brazil-Malvinas Confluence (BMC), one of the most intense open-ocean fronts in the world ocean and a site for the formation of intermediate water masses. Here, we provide a comprehensive description of the BMC based on physical and biogeochemical data – hydrographic stations, profiling floats and subsurface drifters – gathered in March 2015. We use these data in order to characterize the impinging and outflowing currents and to describe the cross- and along-frontal thermohaline structure. In addition, we compare the in-situ measurements with both climatological data and the Mercator Ocean eddy-resolving reanalysis. The hydrographic sections illustrate the contrasting properties between the two western boundary currents: warm, salty, nutrient- and oxygen-poor oligotrophic subtropical waters carried southward by the BC and the cold, fresh, oxygen- and nutrient-rich subantarctic waters carried northward by the MC. The frontal system is also characterized by the presence of thermohaline intrusions, with the cross-frontal gradients and along-front velocities sharpening as the colliding currents shape the frontal system. We also observe brackish waters spreading on top of the frontal jet as a result of both the confluence dynamics and off-shelf advection favored by north-easterly winds. These low-salinity waters are positively correlated with surface ageostrophic speeds over the frontal jet. The cruise data illustrates the high regional and mesoscale variability as compared with climatological conditions, and further document the submesoscale subsurface complexity, which is not properly captured by available operational models.

1. Introduction

The continental shelf and slope circulation of the southwest South Atlantic Ocean has significant implications in the biogeochemistry and water mass structure of the entire South Atlantic basin. This significance arises from exchanges between subantarctic and subtropical waters and between shelf and deep-ocean waters, which lead to high primary production and intense water mass transformations (Jullion et al., 2010; Valla and Piola, 2015; Combes and Matano, 2018; Orúe-Echevarría et al., 2019b). Recent observational and numerical analyses suggest that the water masses transformed within the BMC are significant contributors to the northward flowing limb of the Atlantic Meridional Overturning circulation (Bower et al., 2019; Rühs et al., 2019).

* Corresponding author.
** Corresponding author.
E-mail addresses: dorleta.orue@gmail.com (D. Orúe-Echevarría), pelegri@icm.csic.es (J.L. Pelegrí).

https://doi.org/10.1016/j.dsr.2021.103533
Received 28 September 2020; Received in revised form 19 March 2021; Accepted 30 March 2021
Available online 14 April 2021

List of geographic acronyms

AAIW	Antarctic Intermediate Water
ACC	Antarctic Circumpolar Current
BC	Brazil Current
BCF	Brazil Current Front
BCO	Brazil Current Overshoot
BMC	Brazil-Malvinas Confluence
BMCF	Brazil-Malvinas Confluence Front
MC	Malvinas Current
MRC	Malvinas Return Current
NADW	North Atlantic Deep Water
PPW	Plata Plume Water
RdlP	Rio de la Plata
SAC	South Atlantic Current
SAF	Subantarctic Front
SAMW	Subantarctic Mode Water
SASW	Subantarctic Shelf Water
STMW	Subtropical Mode Water
STSF	Subtropical Shelf Front
STSW	Subtropical Shelf Water
TIC-MOC	Tipping Corners in the Meridional Overturning Circulation
TW	Tropical Water
UCDW	Upper Circumpolar Deep Water

The regional circulation over the shelf and in the open ocean is modulated by the opposing flows of the two western boundary currents (Palma et al., 2008; Matano et al., 2010): Malvinas Current (MC) and Brazil Current (BC). Both boundary currents flow close to the shelf break until their collision at around 38°S, bringing an intense thermohaline front known as the Brazil-Malvinas Confluence (BMC) (Gordon and Greengrove, 1986). Downstream the Confluence, the MC splits in an inner branch flowing north beneath the BC (MC subsurface northward branch; Artana et al., 2019) and an offshore branch turning south in a cyclonic loop, identified as the Malvinas Return Current (MRC; Piola et al., 2013), whereas the BC continues south together with the MRC and finally retroflects at about 45°S towards the northeast (Brazil Current Overshoot, BCO; Saraceno et al., 2004). Following this retroflection, the BCO splits into two branches: one continues northward offshore the BMC (BC offshore recirculation; Valla et al., 2018) while the other flows east forming the South Atlantic Current (SAC) (Stramma and Peterson, 1990) (Fig. 1a).

The MC and BC outline the path of two frontal systems, the Subantarctic Front (SAF) and the Brazil Current Front (BCF), respectively, which might converge forming a single front at the BMC (BMCF) (Saraceno et al., 2004; Barré et al., 2006) (Fig. 1a). The SAF corresponds to the northern branch of the Antarctic Circumpolar Current (ACC) system (Orsi et al., 1995) while the BCF defines the southern limit of the BC (Roden, 1986). The BMCF extends from the shelf-break into the deep

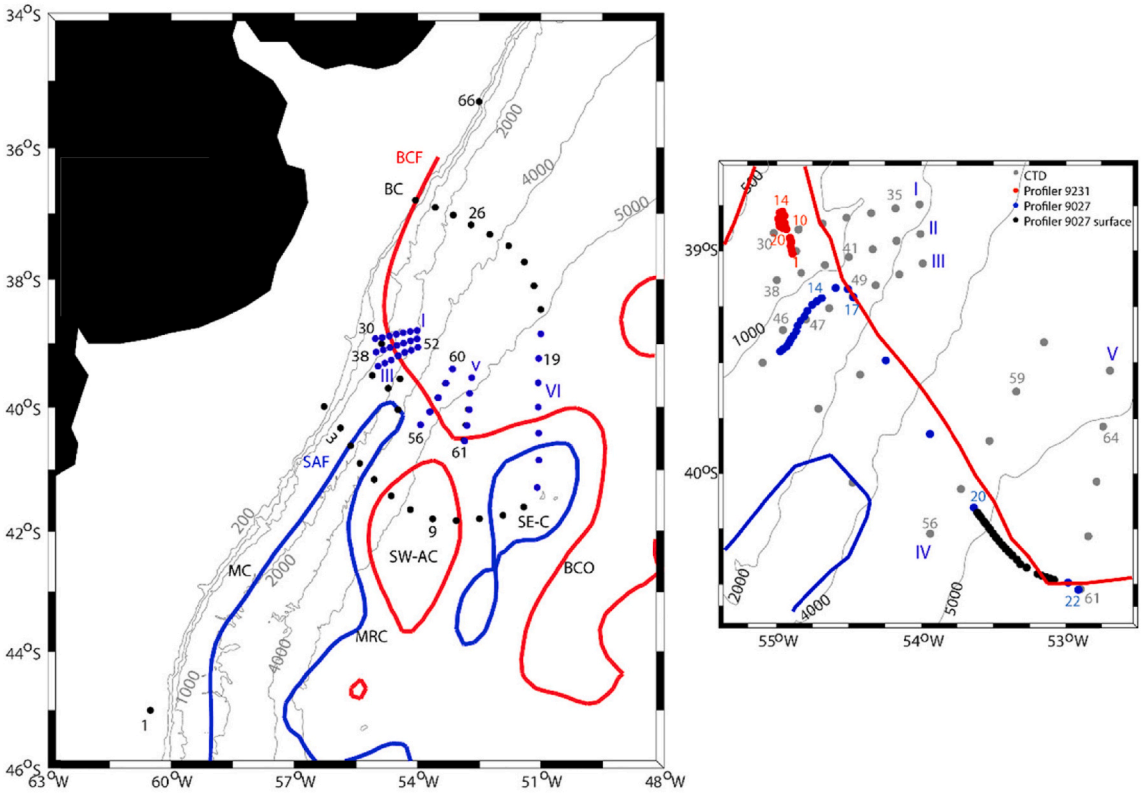

Fig. 1. (a) CTD stations occupied during the TIC-MOC cruise. Red (blue) lines represent the mean March 2015 position of the BCF (SAF) as defined by the 0.30 m (−0.05 m) absolute dynamic topography (ADT) contours (Ferrari et al., 2017). The main currents are indicated: Brazil Current (BC), Brazil Current Overshoot (BCO), Malvinas Current (MC), Malvinas Return Current (MRC). SW-AC and SE-C indicate the position of the main anticyclonic and cyclonic eddies sampled during the cruise, respectively. The black dots represent the stations over the outer perimeter and the blue dots indicate the cross-frontal sections, with the eastern ones also being part of the outer perimeter. Roman/Arabic numbers show the sections/stations. Grey lines represent the 200, 500, 1000, 2000, 4000 and 5000 m isobaths (GEBCO 2008 bathymetry). (b) Cross-frontal CTD sections (black dots), positions of the profiles from floats 9231 (magenta dots) and 9027 (green dots), and surface positions provided by float 9027 between profiles 20 and 21 (cyan dots). The red and blue lines represent the BCF and SAF.

ocean at about 36°S, creating a sharp transition between waters of subtropical and subantarctic origin; this transition over the shelf has also been referred to as the Subtropical Shelf Front (STSF) (Piola et al., 2000).

The encounter of the subtropical and subantarctic water masses at the BMC region generates a complex vertical thermohaline front (Provost et al., 1995), depicted by the interleaving of different water masses (Bianchi et al., 1993). Furthermore, the retroflection of each of the currents results in the creation of structures of multiple scales, such as eddies and filaments (Legeckis and Gordon, 1982; Garcia et al., 2004; Barré et al., 2006; Lentini et al., 2006). One outcome of these interleaving structures is the enhancement of isopycnal and diapycnal mixing between the water masses converging at the BMC (Bianchi et al., 1993, 2002; Garzoli and Matano, 2011; Gaube et al., 2014; Mason et al., 2017; Orúe-Echevarría et al., 2019b).

The BMC is also a preferential site for the exchange of properties across the shelf (Franco et al., 2018). The shelf waters in this region are mainly a mixture of Subantarctic Shelf Water (SASW), a variety of subantarctic water flowing north along the Patagonian shelf, and Subtropical Shelf Water (STSW), which is South Atlantic Central Water (SACW) diluted by continental runoff along the Brazilian coast. On top of these waters, we find a plume of brackish waters associated with the Rio de la Plata (RdlP) discharge. The cross-shelf exchanges promote the export of organic matter, inorganic nutrients, high chlorophyll waters and planktonic species, among other properties, to the open ocean (Combes and Matano, 2014a, 2018; Matano et al., 2014; Franco et al., 2018). This contributes to fertilize the western South Atlantic and therefore to the high biological activity and fisheries in this region (Piola et al., 2010; Berden et al., 2020).

The along-shelf extension of the RdlP plume presents high seasonality, associated with changes in the along-shore winds (Piola et al., 2005, 2008b; Palma et al., 2008). In fall-winter, the along-shore northeastward winds drive the RdlP waters to the northeast in a narrow region close to the coast, beyond 28°S (Piola et al., 2000). Reversely, in spring-summer the southwestward prevailing along-shore winds, advect waters to the southwest, into a broader region that extends nearly 300 km south of the mouth of the estuary (Guerrero and Piola, 1997; Piola et al., 2010), which are eventually exported to the open ocean in the vicinity of the BMC (Piola et al., 2008a; Simionato et al., 2001;Guerrero et al., 2014). This southward displacement of the RdlP during spring-summer waters coincides with a southern position of the BMC over the shelf-break, which reaches its northernmost position in winter (Olson et al., 1988; Wainer et al., 2000; Goni and Wainer, 2001).

Measurements in the BMC date back to the 1980s, when the R/V Atlantis II cruise 107–3 (Gordon, 1981) and Marathon cruises 7-8-9 were carried out (October-November 1984) (Gordon, 1989). About six years later, another intense study was completed, with three surveys done from November 1988 to February 1990 through the Confluence Program (Confluence Principal Investigators, 1990). These field data were used to characterize the spring (Gordon, 1989) and summer (Provost et al., 1995) conditions, including the heat and salt fluxes (Bianchi et al., 1993, 2002), current velocity and transports (Gordon and Greengrove, 1986; Peterson, 1992; Garzoli, 1993; Maamaatuaiahutaou et al., 1998; Vivier and Provost, 1999b), and water masses (Maamaatuaiahutaou et al., 1992, 1994).

Motivated by the high productivity associated to shelf-break upwelling (Acha et al., 2004; Saraceno et al., 2005; Romero et al., 2006; Dogliotti et al., 2014) and its relevance in the biogeochemical carbon cycle (Bianchi et al., 2009; Kahl et al., 2017), most studies have focused on the shelf and upper slope (e.g. Piola et al., 2000; 2005; 2010; Möller et al., 2008; Valla and Piola, 2015; Carranza et al., 2017) and fewer studies have addressed the open-ocean circulation. In the early 1990's and 2000's, and recently between 2013 and 2017, several moorings were installed in the northern and southern margins of the BMC in order to study the variability of the BC (34.5°S) (Meinen et al., 2012, 2013, 2017, 2018; Valla et al., 2018) and MC (41°S) (Vivier and Provost, 1999a; Spadone and Provost, 2009; Ferrari et al., 2017; Artana et al., 2018a; Paniagua et al., 2018). Other studies have dealt with the surface dynamics at the BMC based on satellite data (e.g. Saraceno et al., 2004; 2005; Barré et al., 2006; Lumpkin and Garzoli, 2011; Saraceno and Provost, 2012; Strub et al., 2015) and both regional and general circulation models (e.g. Matano et al., 1993; Palma et al., 2004; Fetter and Matano, 2008; Combes and Matano, 2014a,b; Matano et al., 2014; Artana et al., 2018b, 2019).

Following the 1980s and 1990s surveys, the 2015 TIC-MOC cruise was a renewed effort to produce a quasi-synoptic survey of the BMC, aimed at providing a high-resolution *in situ* picture of the physical and biogeochemical frontal structure and dynamics during the cruise, which could be compared and complemented with the information provided by satellite, reanalysis and climatological data. In section 2 we describe the field, reanalysis and climatological datasets. In section 3 we use the remote sensing and cruise data to describe the surface and three-dimensional (3D) structure of the frontal system. In section 4 we compare the cruise observations with the reanalysis and climatological data and further explore the sources of surface and subsurface variability at the BMC. Finally, the conclusions are presented in section 5.

2. Data

2.1. Field measurements

Hydrographic data were gathered between March 8 and 22, 2015, during the oceanographic TIC-MOC cruise on board R/V Hespérides. Fig. 1a shows the location of the 66 hydrographic stations, which comprise five interior sections and one outer section, and the position of the frontal systems at the time of the cruise. Throughout this study, we will distinguish three regions for our analysis: (1) the outer section, formed by 28 stations in a nearly circular perimeter delimiting the BMC (Fig. 1a); (2) the near field, formed by the three westernmost cross-frontal interior sections (sections I-III, Fig. 1b); and (3) the far field, which includes the two eastern cross-frontal interior sections (sections IV-V, Fig. 1b) plus seven stations along the meridional section of the outer perimeter (section VI along 51°W, Fig. 1a). In the outer perimeter, the stations are spaced about 45 km and sampling reaches down to the sea floor over the upper slope or down to 2000 m in the open ocean. Each of the interior cross-frontal sections has a length of approximately 100 km, with stations spaced about 15 km and sampling down to the sea floor over the slope or down to 400/500 m in the near/far field sections. We next present a brief description of both the cruise and the methodology for data acquisition and processing. Further information can be found in Orúe-Echevarría et al. (2019a) and the data are available in Pelegrí et al. (2018).

At each of the 66 hydrographic stations, a conductivity-temperature-depth (CTD) cast was performed with a CTD SBE 911+ instrument, with redundant salinity and temperature sensors and additionally equipped with a SBE 43 oxygen sensor. The CTD data were processed according to common standards and subsequently vertically-averaged at 1-dbar pressure intervals. At each station, water samples were collected at standard depths to determine nitrate (NO_3^-), phosphate (PO_4^{-3}) and silicate (SiO_4^{2-}) concentrations.

Throughout the cruise, continuous vertical profiles of horizontal current from 20 m to around 700 m, in 8-m depth bins, were obtained with the vessel's hull-mounted Acoustic Doppler Current Profiler (VADCP). Raw data were quality controlled, corrected and edited with the Common Oceanographic Data Access System (CODAS, Firing et al., 1995). Additionally, a thermosalinograph provided continuous near-surface (about 5 m depth) temperature and salinity data from the vessel's underway system.

With the objective of obtaining a detailed description of the thermohaline structure of the BMCF, two Apex-type profiling floats (identified as 9027 and 9031) were deployed (Fig. 1b). Both floats were

equipped with a SBE 41CP CTD, enabling to monitor water-mass properties along their journey. Float 9027 completed 22 profiles in 9 days while float 9231 did 20 profiles in 7 days; both floats cycled in continuous mode, with relatively shallow (300–500 m) initial profiles that eventually stabilized at 700–800 m. The parking depth of the profilers varied between 200 m (profiles 1–14 of float 9027 and profiles 1–10 of float 9231) and 1000 m (profiles 15–22 of float 9027 and profiles 11–21 of float 9231).

The trajectory of float 9027 was peculiar and deserves a brief mention. After profile 17, the communication with float 9027 was lost for two days. During that period, the float performed two additional (non-positioned) profiles. The communication and positioning data were recovered for the 20th profile on. We estimate the location of these two non-positioned profiles by using the location of profiles 17 and 20 and the time spent between them. Between profiles 20 and 21 the float drifted at the sea surface, providing 33 additional positions.

Finally, eight subsurface drifters were launched in order to track the near-surface waters in the frontal area (six dragged at 100 m and two dragged at 200 m). Four drifters were equipped with Global Star satellite data transmitter and the other four had Iridium transmitters; drifting positions were acquired at intervals of 30 min.

2.2. Remote sensing data

A description of the sea-surface conditions in the entire region is obtained with sea surface temperature (SST) and altimetry satellite products. SST corresponds to 1/4°-gridded 7-day averaged Advanced Microwave Scanning Radiometer (AMSR-2) images. Satellite altimetry data corresponds to the delayed-time DUACS altimeter gridded product Pujol et al., 2016 provided by Copernicus Marine and Environment Monitoring Service (CMEMS) (daily 1/4° Mercator grid, multi-satellite, delayed-time product), which includes absolute dynamic topography (ADT) and surface geostrophic velocity. We use the ADT field to identify the location of the BCF (ADT = 0.30 m) and SAF (ADT = −0.05 m) (Ferrari et al., 2017).

2.3. Climatological and reanalysis data

A climatological view of the study region is available from the World Ocean Atlas v.2 (WOA13), which provides monthly-mean fields of temperature and salinity at 69 vertical level (0–5600 m) for the global ocean at 1/4° resolution on a Mercator grid (Locarnini et al., 2013; Zweng et al., 2013).

High-resolution operational CMEMS model PSY4QV2R2 predictions for ADT and SST – as well as for temperature, salinity and velocity at 0, 92, 453 and 1062 m – were received on board during the TIC-MOC cruise. These data were fundamental for the cruise design, particularly in estimating the preliminary location of the frontal system. Rather than model predictions, here we use the GLORYS12V1 reanalysis product (hereafter simply GLORYS or reanalysis), largely based on the CMEMS forecasting system. The data is provided daily with a spatial resolution of 1/12° grid and 50 standard vertical levels, from the sea surface down to 5500 m. The reanalysis is based on the NEMO3.1 numerical model forced at the surface with the European Centre for Medium-Range Weather Forecasts (ECMWF) ERA-Interim reanalysis, which assimilates in-situ temperature and salinity profiles, SST from the 1/4° resolution Advanced Very High Resolution Radiometer (AVHRR) and along-track altimetry data. Artana et al. (2018b; 2019) have compared this reanalysis with in-situ measurements, concluding that it correctly reproduces the large-scale circulation at the BMC.

Finally, we use the daily-mean Cross-Calibrated Multi-Platform (CCMP, Atlas et al., 2011) winds with a 25 × 25 km resolution, from the 1st January to the end of March 2015. This wind dataset has shown to have a good correspondence with in-situ measurements at the BMC, being able to capture the high wind variability in this region (Carranza et al., 2017).

3. Results

3.1. Surface fronts

A surface view of the Confluence area for March 2015 is shown in Fig. 2. Both the reanalysis and satellite fields illustrate the complex surface dynamics of the BMC. The northern half of the outer section is within the relatively warm and saline waters of the BC. In the southern sector, the four western stations are characterized by cold and fresh MC waters. East from the MC, there is a warm and salty anticyclonic ring (SW-AC) followed by a cyclonic eddy (SE-C) with subantarctic waters that contribute to the frontal jet (Fig. 2b). The SAF reaches approximately 40°S before retroflecting south with the MRC. The surface geostrophic and in-situ velocity fields identify the colliding BC and MC as well as the eastward resulting frontal jet (Fig. 2b,g,h).

Sea surface salinity (SSS) and SST reanalysis images (Fig. 2c and d) identify the MC as relatively cold, fresh and dense waters flowing northward along the Patagonian shelf-break until the BMC region, located at about 39.5°S. At this latitude, the MC encounters higher ADT, SST and SSS values that characterize the subtropical waters to the north of the BCF. The ADT differences between the BCF and SAF (0.35 m) match SST and SSS differences of about 8.0 °C and 2.0, respectively. The satellite and reanalysis images in Fig. 2 show data for March 17, 2015, when the sampling of the interior cross-frontal sections began (the SST/SSS evolution before and during the entire cruise are available in Figs. S1 and S2, Supplementary materials).

The model's mesoscale fields are very similar to the patterns observed via remote sensing, as expected from the model's assimilation of these satellite datasets (Fig. 2). However, there are also some significant differences. First, the reanalysis shows submesoscale structures of a few tens of kilometers, such as small vortices and narrow filaments observed southeast of the BMC, which are not visible in the infrared and altimetry data (their absence in the high-resolution SST data is probably because of cloudy conditions over the frontal region). Second, while the BCF position is almost the same in the altimetry and reanalysis maps, the location of the SAF is about 75 km further south in the reanalysis than in the altimetry one. Additionally, the subtropical waters (SST > 23.0 °C) extend further south in the satellite than in the reanalysis, and the cross-frontal temperature gradients are less intense in the satellite than in the reanalysis (0.12 °C km^{-1} and 0.30 °C km^{-1}, respectively), despite the satellite suggests a greater northward penetration of the MC along the slope.

In the reanalysis image, we identify a plume of low-salinity water (S < 34.0), associated with the RdlP and SASW waters extending offshore along the frontal jet. The northern edges of the interior cross-frontal sections are within this plume, which allows us to characterize its dimensions (sections 4.1 and 4.2). The near-surface salinity measured along the cruise-track (Fig. 2h) is consistent with the reanalysis SSS image. As expected, the WOA13 data (Fig. 2e and f) shows temperature and salinity fields much smoother than either the satellite or the reanalysis, displaying the main currents and frontal patterns at positions different from the other datasets.

3.2. Frontal system

We present cross-frontal sections of salinity (S) and potential temperature (θ) (Fig. 3), dissolved oxygen (DO) and silicate (SiO_4^{2-}) (Fig. 4), nitrate (NO_3^-) and phosphate (PO_4^{3-}) (Fig. 5), and horizontal water velocity (Fig. 6) for the outer, near-field and far-field sections.

3.2.1. Outer section

The outer perimeter of the BMC displays substantial property changes in the upper 800 m. These contrasts are evident both in the BMCF and between the eddies' cores and the surrounding waters (Fig. 3a). The SW-AC, centered near station 9, contains subtropical origin waters, as this eddy detached from a meander of the BCF

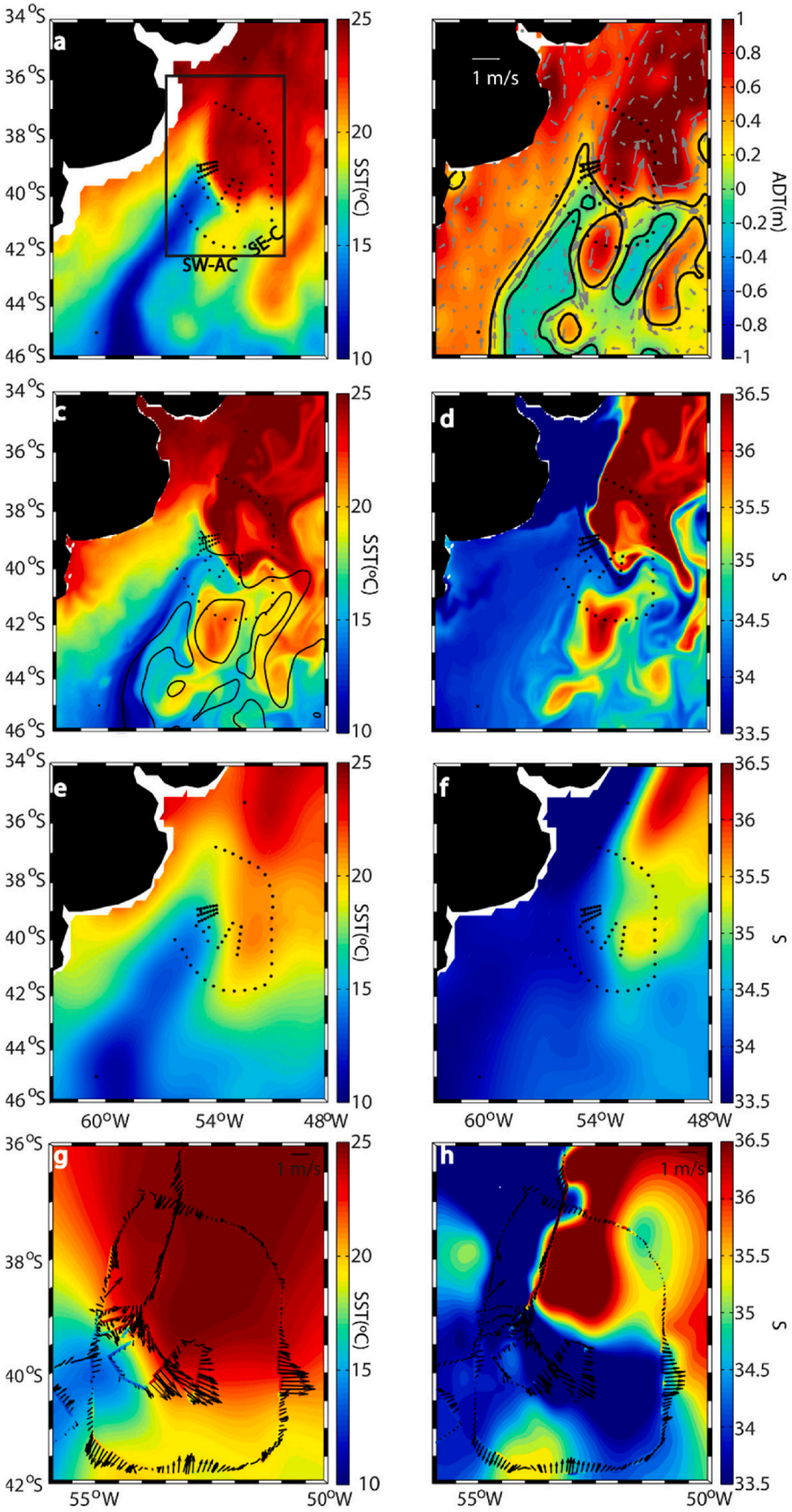

Fig. 2. (a) Satellite SST (°C) and (b) satellite ADT (m) and geostrophic velocity on March 17, 2015. (c) SST and (d) SSS from reanalysis data on March 17, 2015. (e) SST and (f) SSS March-mean fields from WOA13. (g) SST and (h) SSS from the TIC-MOC thermosalinograph data interpolated into the area highlighted in the rectangle in panel a; the vectors show the VADCP velocity (g) at 20 m and (h) averaged in the upper 700 m. The black dots represent the position of the CTD casts during the TIC-MOC cruise, and the black contours in (b,c) show the position of the SAF and BCF (−0.05 and 0.30 m ADT contours, respectively).

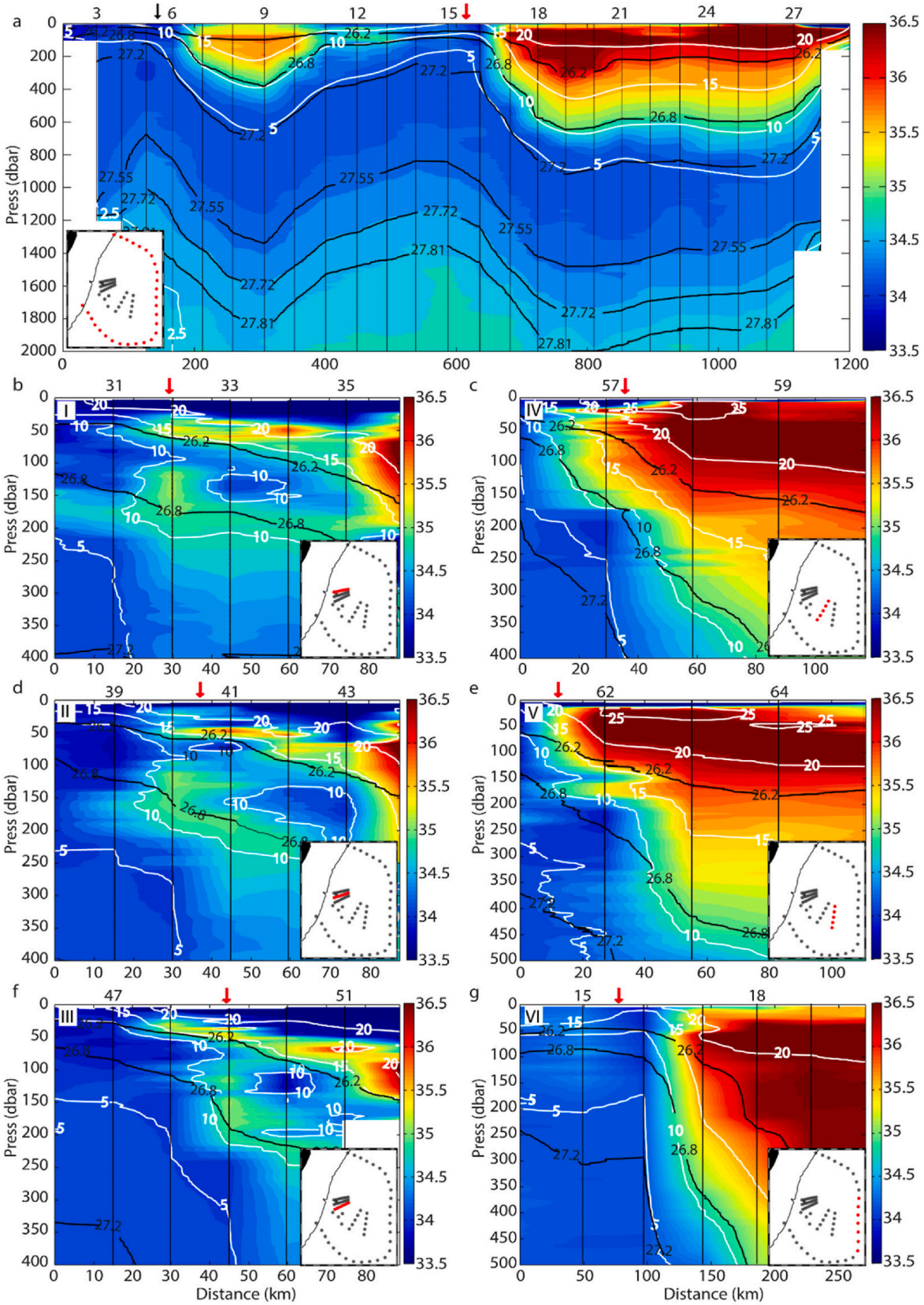

Fig. 3. Vertical sections of salinity (colored), potential temperature (white contours, °C) and neutral density (black contours, kg m^{-3}): (a) outer section, (b, d, f) near-field sections (I-III), and (c, e, g) far-field sections (IV-VI). The top numbers locate the stations and the black dots the measurement depths, and the Roman numbers denote the sections, as in Fig. 1. The black and red arrows indicate the mean position of SAF and BCF for March 2015, respectively, as defined following satellite-derived ADT criteria. The inlet figures highlight in red the stations included in each section. The origin of the outer section is set at the shelf station to the southwest; for the remaining sections the origin is set at the southernmost station.

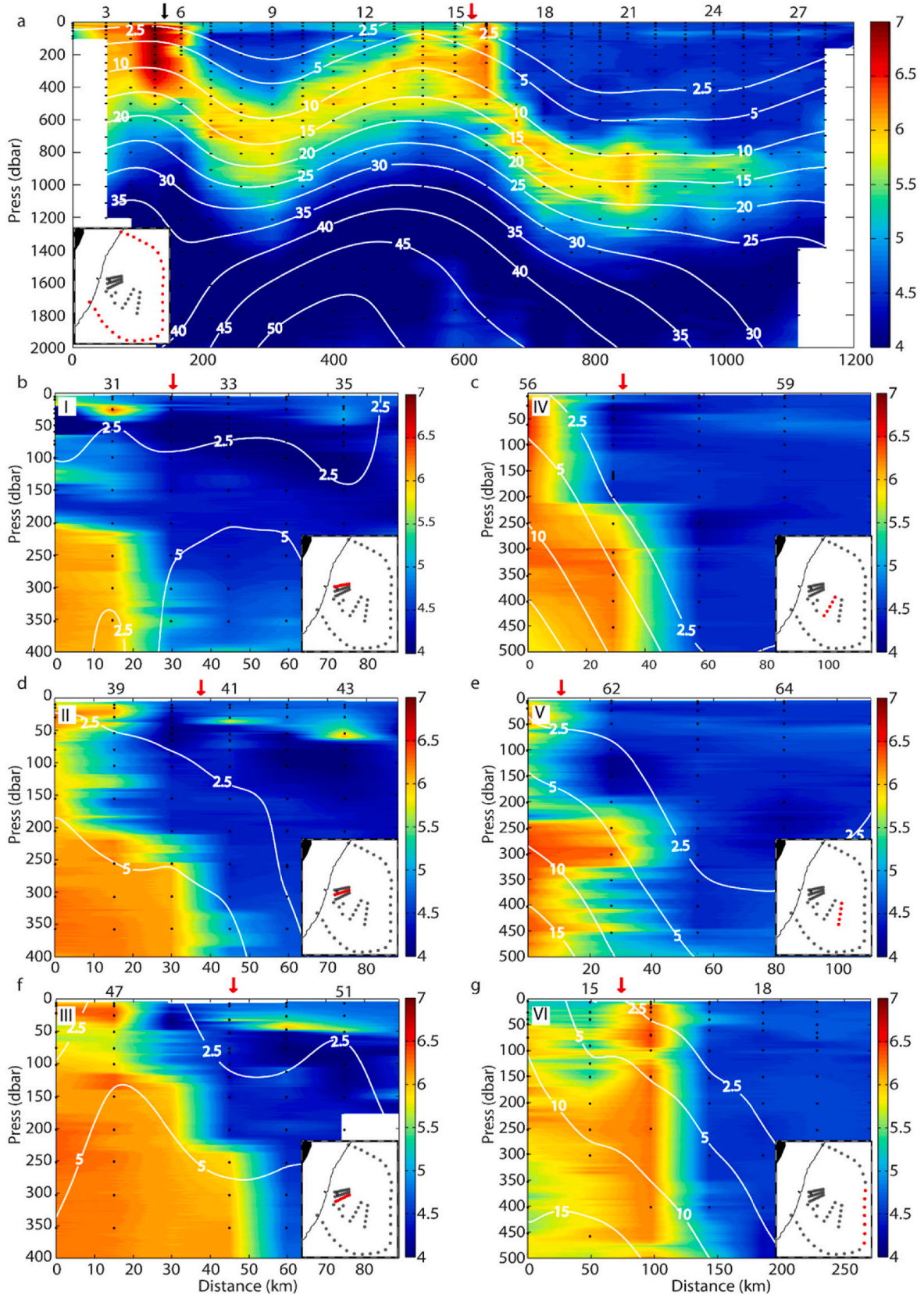

Fig. 4. Vertical sections of concentrations of DO (colored, ml l^{-1}) and SiO^{2-} (white contours, μmol l^{-1}): (a) outer section, (b, d, f) near-field sections (I-III), and (c, e, g) far-field sections (IV-VI). The top numbers locate the stations and the black dots the SiO^{2-} measurement depths; the DO measurement depths are those shown for *S* (Fig. 3), and the Roman numbers denote the sections, as in Fig. 1. The black and red arrows indicate the mean position of SAF and BCF for March 2015, respectively, as defined following satellite-derived ADT criteria. The inlet figures highlight in red the stations included in each section. The origin of the outer section is set at the shelf station to the southwest; for the remaining sections the origin is set at the southernmost station.

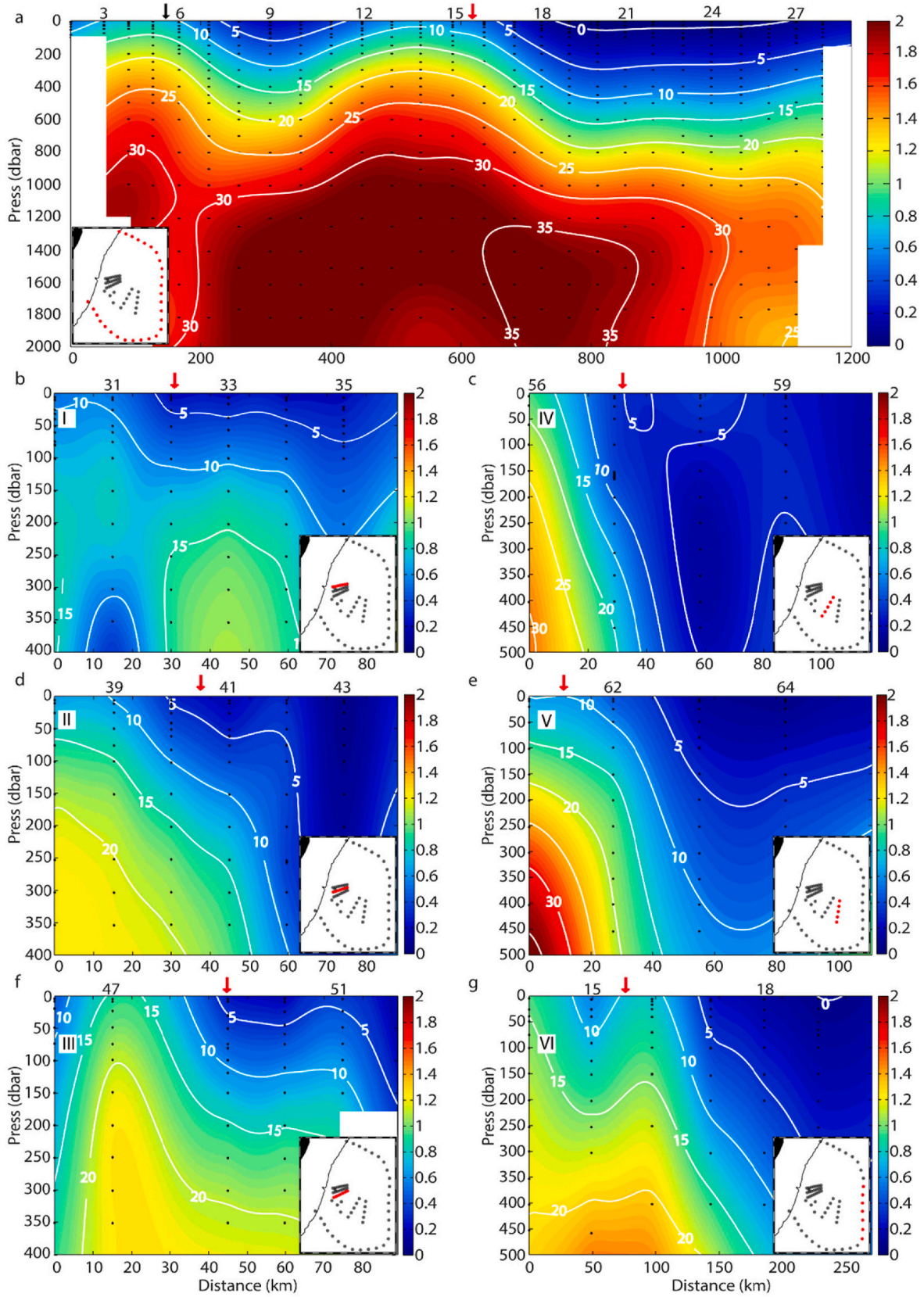

Fig. 5. Vertical sections of concentrations of PO_4^{3-} (colored, μmol l^{-1}) and NO_3^-(white contours, μmol l^{-1}): (a) outer section, (b, d, f) near-field sections (I-III), and (c, e, g) far-field sections (IV-VI). The top numbers locate the stations and the black dots the measurement depths, and the Roman numbers denote the sections, as in Fig. 1. The black and red arrows indicate the mean position of SAF and BCF for March 2015, respectively, as defined following satellite-derived ADT criteria. The inlet figures highlight in red the stations included in each section. The origin of the outer section is set at the shelf station to the southwest; for the remaining sections the origin is set at the southernmost station.

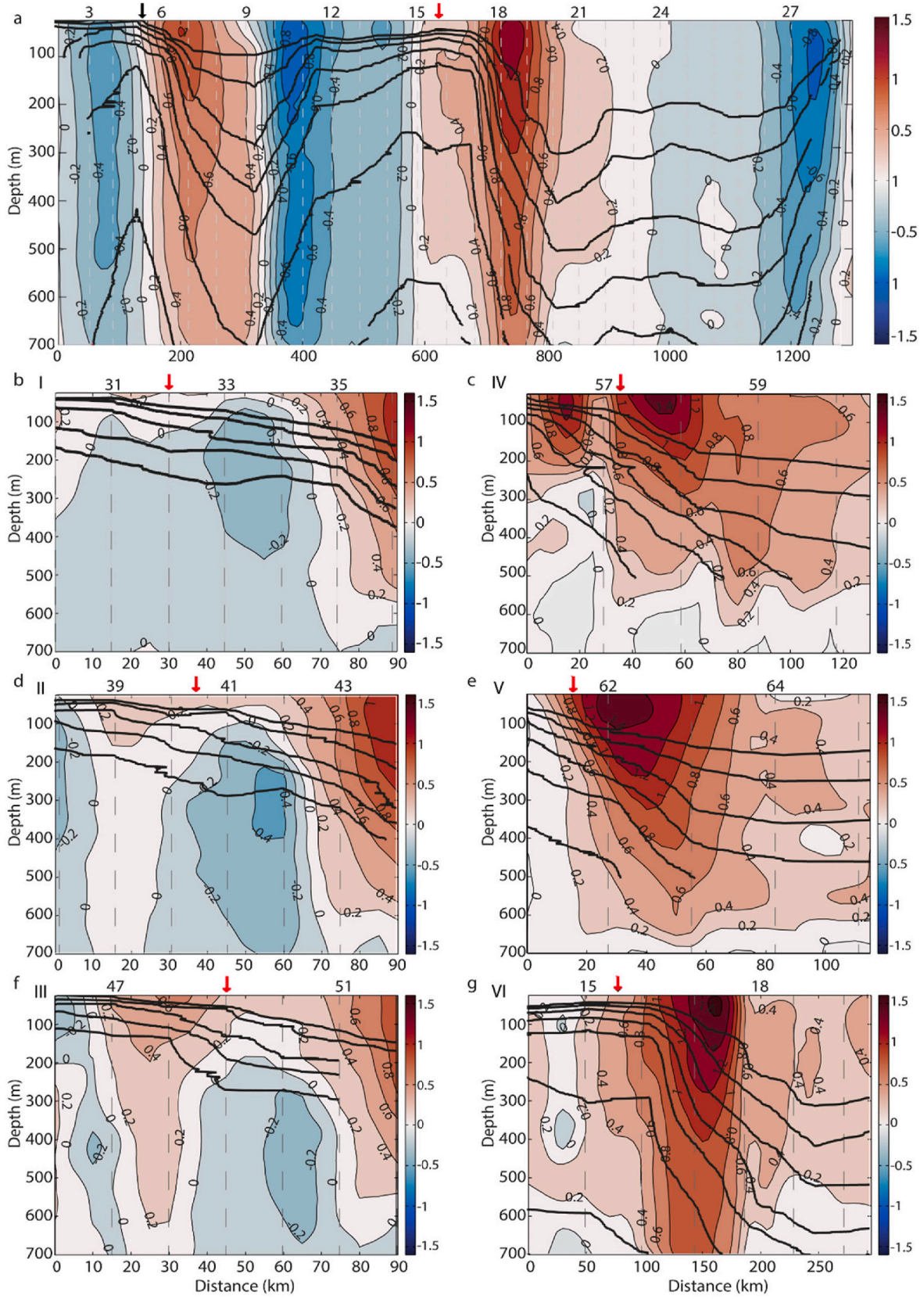

Fig. 6. Absolute speed normal to the section as measured by the VADCP (colored, m s^{-1}) and neutral density (black contours, starting at 26.2 kg m^{-3} every 0.2 kg m^{-3}): (a) outer section, (b, d, f) near-field sections (I-III), and (c, e, g) far-field sections (IV-VI). In the outer section, negative/positive values indicate flow into/out of the BMC; in the cross-frontal sections, positive/negative values indicate eastward/westward flow. The top numbers locate the stations, and the Roman numbers denote the sections, as in Fig. 1. The black and red arrows indicate the mean position of SAF and BCF for March 2015, respectively, as defined following satellite-derived ADT criteria. The origin of the outer section is set at the shelf station to the southwest; for the remaining sections the origin is set at the southernmost station.

(Orúe-Echevarría et al., 2019b). This eddy has a radius of around 200 km and extends down to at least 1800 m; its core has θ/S values of 17.0 °C/35.8 at 100 m, about 8.0 °C/1.0 warmer/saltier than the neighboring waters at that depth. The SE-C, centered near stations 13–14, presents a water mass structure similar to the MC core (stations 3–5, Fig. 3a), cold and fresh (θ/S values of 7.2 °C/34.3 at 100 m), though slightly saltier and warmer as a result of mixing at the BMC and the incorporation of warmer waters recirculating around the BCO (Orúe-Echevarría et al., 2019b). In the meridional section along 51°W, we can identify the BMCF at approximately 40°S-51°W (stations 16–17, Fig. 3a), where θ/S changes from 5.0 °C/34.2 to 17.0 °C/36.1 within 50 km in the upper 500 m. Below 800 m, both temperature and salinity differences are much reduced, though the isopycnals have slopes comparable to the upper layers.

We also use θ-S diagrams (Fig. 7), with the help of the reference density-range definitions, in order to identify the different water masses (Valla et al., 2018; Orúe-Echevarría et al., 2019b) (Table 1). In the north-westernmost stations of the outer section (stations 27 and 28), the upper part of the water column is occupied by very low salinity Plata Plume Water of river origin (PPW, $S < 32.5$) (Piola et al., 2008a), SASW flowing along the Patagonian shelf (fresher and warmer than MC waters: $\theta < 21.0$ °C, $S < 34.0$; Piola et al., 2000), and STSW formed north of the SASW as a mixture of river and BC waters ($\theta > 18.5$ °C, $S < 36.0$; Piola et al., 2000; Möller et al., 2008). North of the BMCF, in the upper 100–130 m, we find the warmest ($\theta \cong$ 19.2 °C) and saltiest ($S \cong$ 36.4) Tropical Water (TW). Formed at tropical latitudes and transported south with the BC, the TW is poorly oxygenated (DO $\cong$ 4.6 ml l^{-1}) and nutrient depleted (Worthington, 1976); this water mass was not found south of the BMCF.

The main BMCF contrast occurs in the upper thermocline layers, occupied by the South Atlantic Central Water (SACW). These central waters, present in the 200–600 depth range, are characterized by a nearly straight line in the temperature-salinity diagrams, between (5.0 °C, 34.1) and (17.5 °C, 36.2). They include two mode waters, Subtropical Mode Water (STMW, in the 26.2–26.8 kg m^{-3} neutral-density range) and Subantarctic Mode Water (SAMW, in the 26.8–27.2 kg m^{-3} neutral-density range).

On the northern side of the BCF, we find STMW ($\theta \cong$ 11.0–18.0 °C, $S \cong$ 35.1–36.2) below the TW and down to 500 m; this water mass is not present south of the BCF, except within the SW-AC core. The STMW is formed along the Subtropical Front of the South Atlantic Ocean and at the BCF during austral winter and early spring (Provost et al., 1999). The θ-S diagram shows two inflection sectors, near (17.0 °C, 36.2) and (14.0–16.0 °C, 35.6), each corresponding to a different STMW variety (Fig. 7). Considering the three STMWs defined by Provost et al. (1999) for the South Atlantic, the first sector corresponds to $STMW_1$ ($\theta \cong$ 17.0–18.0 °C, $S > 36.0$), which extends from below the TW down to approximately 250 m, while the second zone corresponds to $STMW_2$ ($\theta \cong$ 14.0–16.0 °C, $S \cong$ 35.5–35.9), which is found immediately below and down to about 500 m. This second sector corresponds also to the STMW Type I defined by Sato and Polito (2014), which is primarily formed in the BMC area.

South of the BCF and below the warm summer mixed-layer, in the core of the MC, waters are dominated by the coldest and freshest variety of mode water, the SAMW ($\theta \cong$ 5.1 °C, $S \cong$ 34.1; Piola and Gordon, 1989). Due to its winter-convection origin in a nutrient-rich region, along the subantarctic zone of the northern Drake Passage (McCartney, 1977, 1982; Palter et al., 2010), these waters have relatively high DO, PO_4^{3-} and SiO_4^{2-} concentrations (about 6.3 ml l^{-1}, 1.8 μmol l^{-1} and 7.5 μmol l^{-1}, respectively). A somewhat saltier ($S \cong$ 34.4), poorer in oxygen and nutrients, variety of SAMW extends north, past the BCF under STMW, at 500–800 m; for example, the DO concentrations in the outer section (along 51°W) are about 5.0–6.0 ml l^{-1}, somewhere in between the SAMW and STMW values (Table 1), clearly reflecting the intense

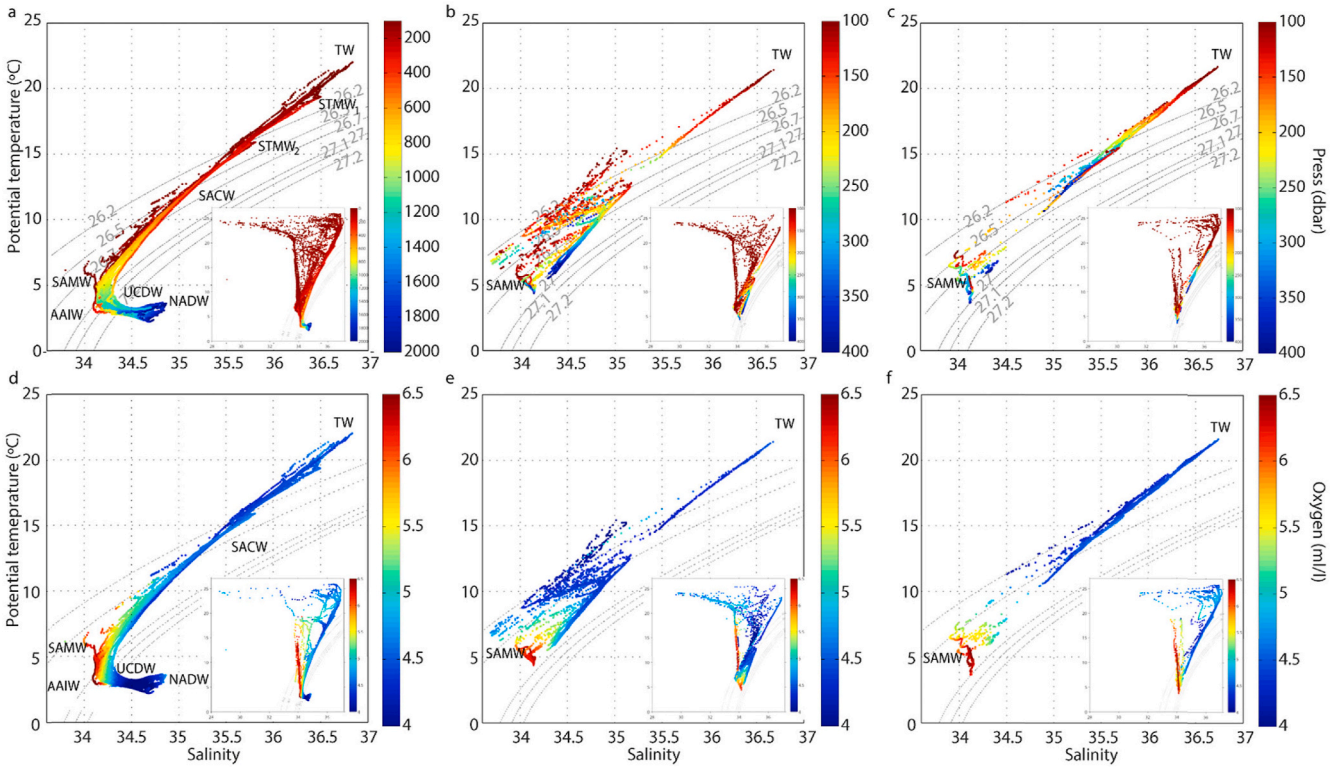

Fig. 7. Potential temperature-salinity (θ-S) diagrams: (a, d) outer section, (b, e) near-field sections (I-III) and (c, f) far-field sections (IV-VI), excluding the upper 100 m; for comparison, the inset diagrams in each panel do include these near-surface data. Colors represents the (a, b, c) pressure (dbar) and (d, e, f) DO concentration (ml l^{-1}) of each point. Grey dotted lines indicate constant potential density. The water masses are: Tropical Water (TW), South Atlantic Central Water (SACW), Subantarctic Mode Water (SAMW), Antarctic Intermediate Water (AAIW), Upper Circumpolar Deep Water (UCDW) and North Atlantic Deep Water (NADW).

Table 1
Average potential temperature (θ), salinity (S), dissolved oxygen (DO), and silicate (SiO_4^{2-}), nitrate (NO^-_3) and phosphate (PO_4^{3-}) concentrations in the main water mass layers at the centre of each neutral density (γ^n) range, as found during the TIC-MOC cruise. Property ranges for each water mass, according to the literature are included in Table S1 (Supplementary material).

Water mass	γ^n (kg m^{-3})	θ (°C)	S	DO (ml l^{-1})	SiO_4^{2-} (μmol l^{-1})	NO^-_3 (μmol l^{-1})	PO_4^{3-} (μmol l^{-1})
TW	<26.2	19.2	36.4	4.6	0.7	0.9	0.1
STMW	26.2–26.8	14.7	35.5	4.5	2.4	9.2	0.6
SAMW	26.8–27.2	6.2	34.3	6.3	7.4	28.0	1.8
AAIW	27.2–27.55	3.6	34.2	5.6	20.5	33.0	2.0
UCDW	27.55–27.92	2.8	34.6	4.0	50.0	38.8	2.2

mixing at the BMCF (Valla et al., 2018; Orúe-Echevarría et al., 2019b).

The intermediate layers (27.20–27.55 kg m^{-3}) are occupied by salinity-minimum Antarctic Intermediate Water (AAIW; $S \cong 34.2$, $\theta \cong 3.6$ °C). The core of this water mass deepens from 200 m in the southern sector to around 1000 m in the northern flank of the BMCF (Fig. 4a). Originating in the southeast Pacific (e.g. Molinelli, 1978; Sloyan et al., 2010), these waters occupy the upper few hundred meters of the MC and subduct as they encounter the BMC (McCartney, 1982; Piola and Gordon, 1989; Talley, 1996; You, 2002). The AAIW is highly modified in the BMC (Sloyan and Rintoul, 2001; Valla et al., 2018; Orúe-Echevarría et al., 2019b), which contributes to their freshening and oxygenation north of the front. Once the AAIW leaves the BMC, one part recirculates northward (Valla et al., 2018) and another continues east with the SAC, mixing in the eastern South Atlantic basin with AAIW from the Indian Ocean, incorporated via the Agulhas Current leakage. After crossing the subtropical gyre, some of these waters return south with the BC (Garzoli and Gordon, 1996; Schmid and Garzoli, 2009; Schmid et al., 2000; Rodrigues et al., 2010). Thus, the relatively salty ($S \cong 34.3$) and low DO ($\cong$ 4.9 ml l^{-1} as compared with values > 5.5 ml l^{-1} south of the BMC) waters near 900 m, at the core of the BC (between stations 27 and 29), correspond to this older AAIW.

Below AAIW, we find Upper Circumpolar Deep Water (UCDW, 27.55–27.92 kg m^{-3}), extending in most of the stations down to 2000 m. It is saltier ($S > 34.3$) and slightly colder ($\theta < 2.9$ °C) than AAIW, characterized by a DO minimum (<4.2 ml l^{-1}) and enhanced nutrient concentrations, especially by high SiO_4^{2-} values ($\cong$ 50.0 μmol l^{-1}). The low DO and high nutrient concentrations respond to the old age of this water mass, having travelled along the ACC from the South Pacific across the Drake Passage and north with the MC (Reid et al., 1977; Peterson and Whitworth, 1989; Tsuchiya et al., 1994). UCDW is slightly fresher and more oxygenated in the core of the BC than in the MC, because of diapycnal mixing with AAIW and North Atlantic Deep Water (NADW) along the South Atlantic basin (Valla et al., 2018). In the deepest stations over the MRC (Station 5–7) and in the SE-C (stations 11 to 15), we find NADW characterized by a salinity maximum below 1800 m ($\theta \cong 3.0$ °C, $S \cong 34.9$, DO $\cong$ 4.6 ml l^{-1}).

South of the BMCF, the velocity record shows the barotropic nature of the MC and associated eddies (Goni et al., 1996; Vivier and Provost, 1999a; Piola et al., 2013), with fairly constant velocities in the upper 600 m. In the core of the MC, the mean velocity is 0.5 m s^{-1} (Fig. 6a), in the range of mean velocities previously measured in the MC (0.2–0.6 m s^{-1}) (Spadone and Provost, 2009; Piola et al., 2013; Paniagua et al., 2018). In the outer margin of the SW-AC – centered at those stations (7 and 11) associated with the MRC – the velocity exceeds 0.8 m s^{-1} in the upper 200 m and remains above 0.6 m s^{-1} down to 600 m. The frontal jet near station 18 presents the most intense flow, above 1 m s^{-1} in the upper 300 m and remaining higher than 0.8 m s^{-1} down to 600 m. North of the BMCF and east of the BC, the current is very weak, not exceeding 0.2 m s^{-1}. The BC extends its main core down to 600 m (Piola and Matano, 2001), with peak subsurface velocities ($\cong$ 0.8 m s^{-1} between 70 and 200 m); the near-surface velocity (0.6 m s^{-1}) is higher but within the range of velocities inferred from drifting buoys (0.4 ± 0.2 m s^{-1}) (Assireu et al., 2003; Oliveira et al., 2009). The mean velocity in the BC core decreases to $\cong$ 0.4 m s^{-1} at 600 m (stations 27–29, Fig. 6a), evidencing the baroclinic nature of this current (Matano et al., 2010).

3.2.2. Near field

The cruise measurements in the near-field cross-frontal sections (I-III, Fig. 3b,d,f) show SST peak gradients that agree fairly well with the reanalysis and satellite images (Fig. 2a,c). In particular, these images locate the southern three stations of each section south of the surface SST front. Using the definitions that set the BMCF at the intersection of the 10 °C isotherm and the 200 m level (Garzoli and Bianchi, 1987) or the crossing of the 26.96 kg m^{-3} isopycnal at 380 m (Artana et al., 2018b), these cross-frontal sections appear to be located precisely over the front. However, the 3D frontal system is fairly complex because of the presence of substantial thermohaline intrusions, most evident in the salinity fields of sections I and II (Fig. 3b,d), where high θ and S subtropical origin waters interleave with fresher subantarctic waters.

The low salinity PPW surface layer ($S < 32.5$) is between 20 and 30 m deep, being thickest near the shelf and 20–40 km to the north of the surface front (Fig. 3). Right under the PPW, we find TW and STSW north of the BMCF (down to 200–250 m, stations 32–37, 41–44, 49–52) and SASW and SAMW south of the BMCF (down to 400 m, stations 30–31, 38–41, 46–49). The southern stations, with waters of subantarctic origin, are characterized by relatively high DO and nutrient concentrations (DO > 5.0 ml l^{-1}, NO_3^-> 26.0 μmol l^{-1}, PO_4^{3-}> 1.6 μmol l^{-1}, Fig. 4b,d,f). In contrast, the northern stations correspond to oligotrophic and poorly oxygenated subtropical waters (DO < 4.5 ml l^{-1}, NO_3^- <10.0 μmol l^{-1}, PO_4^{3-}< 1.2 μmol l^{-1}, Fig. 5,b,d,f).

Surface waters in the northern stations move faster than farther south, 1.2 and 0.2 m s^{-1}, respectively (Fig. 2g). Except for the northernmost two stations in each section, the flow is westward from the surface down to 400 m (Fig. 6b,d,f). This westward flow component can be identified in the altimetry-derived geostrophic surface velocity (Fig. 2b), representing an extension of the MC towards the shelf.

3.2.3. Far field

The satellite and reanalysis SST show differences over the far-field sections (Fig. 2a,c). The southern extreme of these sections, south of the BMCF, appears warmer in the satellite imagery than in the reanalysis fields. The cruise sections show that the differences are associated with the presence of the brackish waters on top of the frontal system and confirm that most stations in the far-field sections belong to the subtropical side of the BMCF; the cruise data also show that the subantarctic sector is sampled in the southern two stations of sections IV and V, being separated by a more vertical and a sharper front than in the near field (Fig. 3c,e).

The property gradients are more intense in the far field than in the near field (e.g. at 100 m the salinity and temperature gradients are 0.2 km^{-1} and 0.3 °C km^{-1} in the far field as compared with no salinity gradients and 0.1 °C km^{-1} in the near field) and there are no outstanding thermohaline intrusions (Fig. 3c,e,g). As in the near-field sections, the PPW ($S < 32.5$) remains on top of the subtropical waters. The layer with river-influence waters progressively thins (about 5–15 m in section IV and less than 10 m in section V, Fig. 3c,e) and narrows as it separates from the source (at 51°W it only appears in the upper few meters of station 20, just north of the BCF; Figs. 2d and 3g).

The stations south of the BCF are occupied by SAMW down to 400 m while north of the BCF, under the PPW, we find salty-warm TW in the top 200 m and STMW below. As occurs in the near field sections, there is an abrupt change in oxygen (Fig. 4c,e,g) and nutrient (Fig. 5c,e,g) concentrations from the southern (DO $>$ 5.5 ml l^{-1}, NO_3^- >30.0 µmol l^{-1}, $PO_4^{3-} > 1.5$ µmol l^{-1}) to the northern ends (DO $<$ 4.5 ml l^{-1}, $NO_3^- <$ 15.0 µmol l^{-1}, $PO_4^{3-} < 1.0$ µmol l^{-1}). There is a slight modification of the water masses along the frontal jet, with the major transformation in the SAMW layer, about 0.05–0.10 saltier in the far field as compared with the near field (the central stations of sections II and V are separated by 170 km). These downstream water-mass changes suggest a significant impact of isopycnal and diapycnal mixing along the frontal path.

The waters in the far field flow eastward from the surface down to 700 m, with peak values at the front (surface velocities exceeding 1.6 m s^{-1}; Fig. 6c,e,g), which is substantially faster than in the near field (maximum surface velocities of 1.0 m s^{-1}). These high speeds are similar to those experienced by RAFOS floats in the frontal jet (Vigan et al., 2000) and by the drifters and floats launched during the TIC-MOC cruise (described in section 3.3). Subsurface velocities are also higher in the far field than in the near field, remaining over 0.6 m s^{-1} in the upper 600 m of the BMCF.

3.3. Along-front description

The drifting buoys and profiling floats deployed on both sides of the BMCF converged into the frontal jet and eventually ran eastward along it, providing an approximate Lagrangian description of the frontal system (Fig. 8a). All units launched at the northern flank of the BMC travelled southward with the BC and ran along the northern border of the BMCF, while those deployed in the southern margin remained mostly south, with only one instance temporarily crossing the front to the north (Fig. 8a).

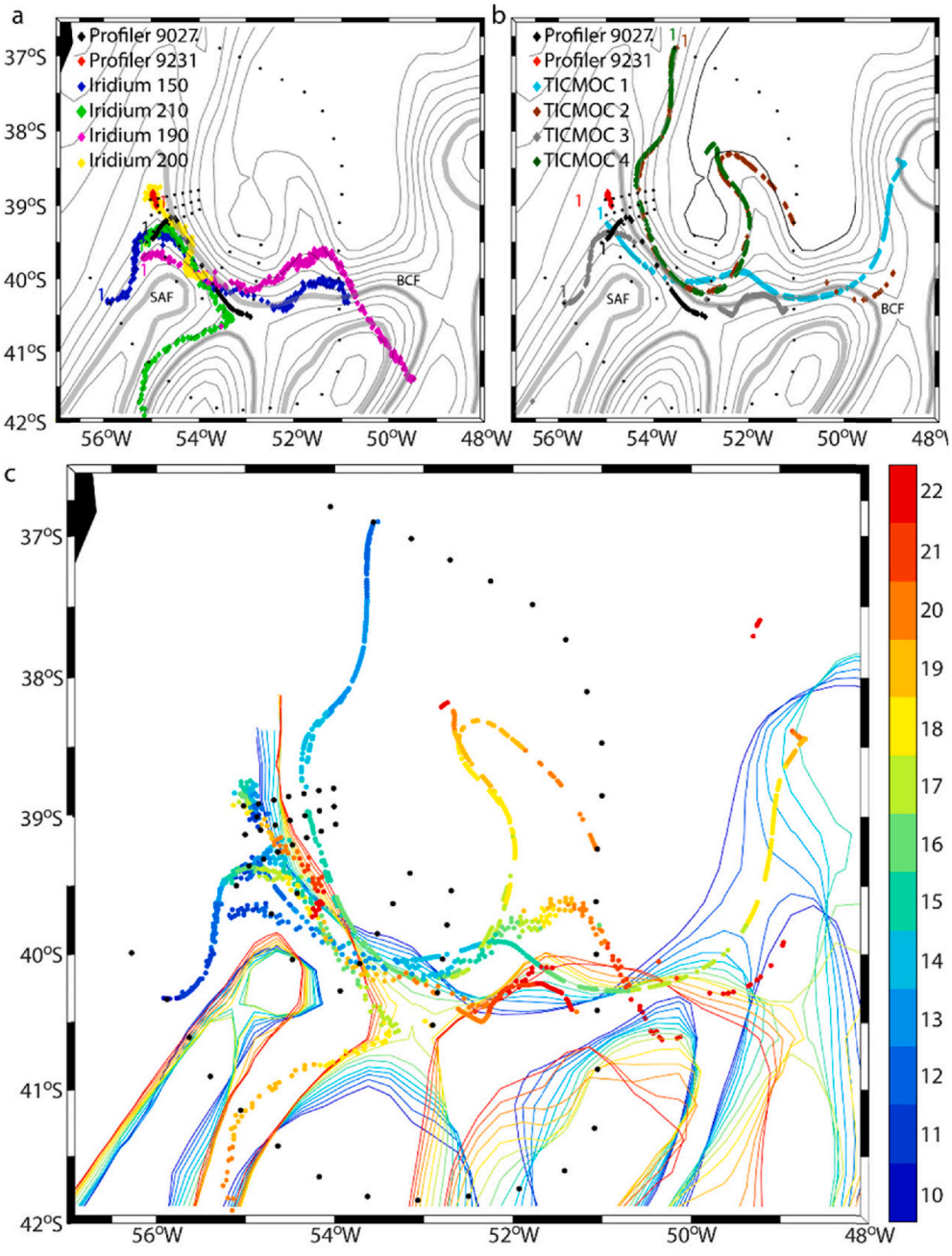

Fig. 8. (a,b) Trajectories of subsurface drifters and profiling floats (colored dots), mean ADT contours (from −0.2 to 0.9 m every 0.1 m; grey contours) and mean location of the SAF and BCF (grey heavy contours) between March 10 and 22, 2015. The starting locations of the trajectories are identified with the digit 1. (c) Trajectories of subsurface drifters and profiling floats (dots) together with the location of the SAF and BCF (northern and southern thin lines, corresponding to ADT = −0.05 and 0.30 m, respectively), color-coded by the day of March. The black dots indicate the location of the CTD stations.

The subsurface buoys travelled along the frontal jet with mean speeds slightly over 0.7 m s^{-1}, exceeding 1.6 m s^{-1} at certain intervals and with peak values of 2.0 m s^{-1} (Table 2). The BMCF is not stationary, fluctuating and undulating during the two weeks of cruise measurements, with the drifters and floats changing their trajectory accordingly. Several drifters were trapped by different mesoscale features, which drove them out of the frontal jet (Fig. 8b, Fig. S3, Supplementary Materials).

The two Apex profiling floats present very different trajectories (Figs. 1b and 8a). Float 9027, which was deployed in the southern edge of the BMCF, drifted northeastward about 55 km across ADT contours and reached the frontal position in three days, moving along the front afterwards. The overall velocity of float 9027 was around 0.2 m s^{-1} south of the BMCF (profiles 1–15, Fig. 9a) and increased to 0.8 m s^{-1} once it reached the front (profiles16-21, Fig. 9a). If we only consider the drifting between profiles 20 and 21, when the float remained at the surface, we get a sustained velocity of about 1.5 m s^{-1}. On the other hand, according to the surface geostrophic velocity fields derived from the satellite ADT, float 9231 was deployed in a region characterized by low westward velocity (not shown). This float moved first westward to later loop anticlockwise until ending up near its initial position, most of the time travelling at speeds less than 0.1 m s^{-1} (Fig. 10a).

The first 14 profiles of float 9027 correspond to the portion of the float trajectory between the SAF and BMCF (Figs. 1b and 8a), across the northernmost extend of the MC, where water properties are homogeneous and there are no subtropical water intrusions (Fig. 9). Between profiles 15 and 17, the float reached the BMCF and stayed very close or even over the frontal jet, in a band where both MC and BC waters coexist, hence explaining the warm and salty intrusions between 80 and 200 m. Most of the structure is confined to the upper 400 m, with thin intrusions that display substantial horizontal coherence. For example, there is an intrusion of STMW at about 180–220 m, stretching for over 100 km between stations 19 and 22. During the along-frontal journey (profiles 15 to 20), the upper 10–20 m are characterized by very low salinity PPW waters, in agreement with the vertical extension of the plume observed in the CTD cross-frontal sections.

On the other hand, float 9231 was deployed in the northern margin of the MC, just upstream of the BCF and close to the shelf break, in some sort of stagnation point in the western margin of the frontal system (Figs. 1b and 8a). As a consequence, this profile ran a short distance, providing a high-resolution perspective of an area that had not yet experienced the collision of the western boundary currents. The upper 40 m present very low salinity SASW followed by a 250-m thick layer of SACW where colder and fresher waters intrude. Below the subsurface salinity maximum (30–70 m) and down to 200–250 m, the water column is dominated by STMW but there are many relatively small intrusions of SAMW (vertical and horizontal extensions of about 50 m and 10 km, respectively). Beyond profile 13, the surface layer of SASW deepens to 60 m, and in profile 15 we find a small double-cored subsurface intrusion of SAMW at about 230 m. The last profile revisited the area between profiles 10 and 11 approximately 4.5 days later. In this second visit, the structure below 150 m remains fairly unchanged but the surface characteristics have changed drastically; in particular, the SASW layer has thickened from 20 to 50 m. Contrary to expectations, considering the proximity to the shelf, the θ-S diagram does not show the presence of PPW (Fig. 10d), though there is a significant presence of SASW. This probably responds to the southern position of the sampling area with respect to the BMCF (Figs. S2–S4, Supplementary materials), suggesting that the float was located far from the main locus of PPW detrainment but close to the SASW detrainment point (Franco et al., 2018).

4. Discussion

4.1. Comparison of cruise, satellite, reanalysis and climatological data

The satellite, reanalysis and in-situ measurements show good overall agreement in the surface fields. This agreement is particularly good between observations and reanalysis, certainly because of the assimilation of satellite data. The high-resolution reanalysis data is able to properly reproduce the PPW on top the frontal jet and matches well the hydrographic SST at each station.

The GLORYS and WOA13 datasets also provide data at 50 and 69 vertical levels, respectively, which can be compared with the TIC-MOC observations. For this purpose, we consider sections II and VI, respectively representing the near and far fields (Fig. 11), and retrieve the corresponding reanalysis outputs by choosing the closest grid points to the CTD stations for the same day of the sampling (March 18 for section II and March 14 for section VI). GLORYS reproduces well the frontal structure and location, and even the presence of PPW in the surface, but fails at replicating the submesoscale features in section II as inferred from the CTD data (despite its horizontal resolution, 1/12°, is better than the 15-km station spacing) (Fig. 11a,c). Regarding section VI, the overall comparison shows similar vertical structures in the observations and reanalysis, a simple consequence of the lack of intrusions in this outer section where the spatial sampling had lower horizontal resolution. However, south of the frontal area, the subsurface waters (100–200 m) are saltier in GLORYS than in the CTD sections. This could be a reanalysis artefact associated to the warm surface PPW waters (Fig. 11b,d). In the case of the climatology, the differences with the observations are very large in both sections; clearly, the monthly fields cannot emulate the BMC short-term variability.

Based on these results, we can conclude that the reanalysis simulates correctly the surface structure of the BMC region, such as the BMCF/BCF location and the presence of the PPW plume on top the frontal jet. However, it does not reproduce the main subsurface characteristics, neither the frontal location nor the submesoscale thermohaline intrusions. As might be expected, the GLORYS reanalysis is useful in studies concerning surface properties and their variability, as suggested by Artana et al. (2018b; 2019), but is a limited tool to identify and analyze subsurface submesoscale or mixing processes close to the sharp BMCF.

4.2. Presence of shelf water

Franco et al. (2018) identified the BMC region as the main detrainment point of SASW into the open ocean, at a rate of about 1 Sv (10^6 m^3 s^{-1}) for early fall. Berden et al. (2020) also find a main branch of SASW exported offshore along the BMC after having mixed with BC waters.

Table 2
Deployment dates and locations, and mean speeds between March 10 and 22, for the surface drifters.

Name	Date (yyyy/mm/dd)	Latitude S	Longitude W	Drogue depth (m)	Mean velocity (m s^{-1})
TICMOC 1	2015/03/11	39°14.85′	54°58.90′	100	0.9 ± 0.5
TICMOC 2	2015/03/12	36°53.93′	53°31.11′	100	1.1 ± 0.3
TICMOC 3	2015/03/10	40°19.80′	55°52.80′	200	0.4 ± 0.3
TICMOC 4	2015/03/12	36°54.39′	53°34.23′	200	0.9 ± 0.4
IRIDIUM 150	2015/03/10	40°18.45′	55°53.18′	100	1.3 ± 0.4
IRIDIUM 190	2015/03/11	39°44.75′	55°12.35′	100	1.4 ± 0.5
IRIDIUM 200	2015/03/11	39°29.50′	55°05.50′	100	1.2 ± 0.4
IRIDIUM 210	2015/03/11	39°00.29′	54°52.25′	100	1.5 ± 0.6

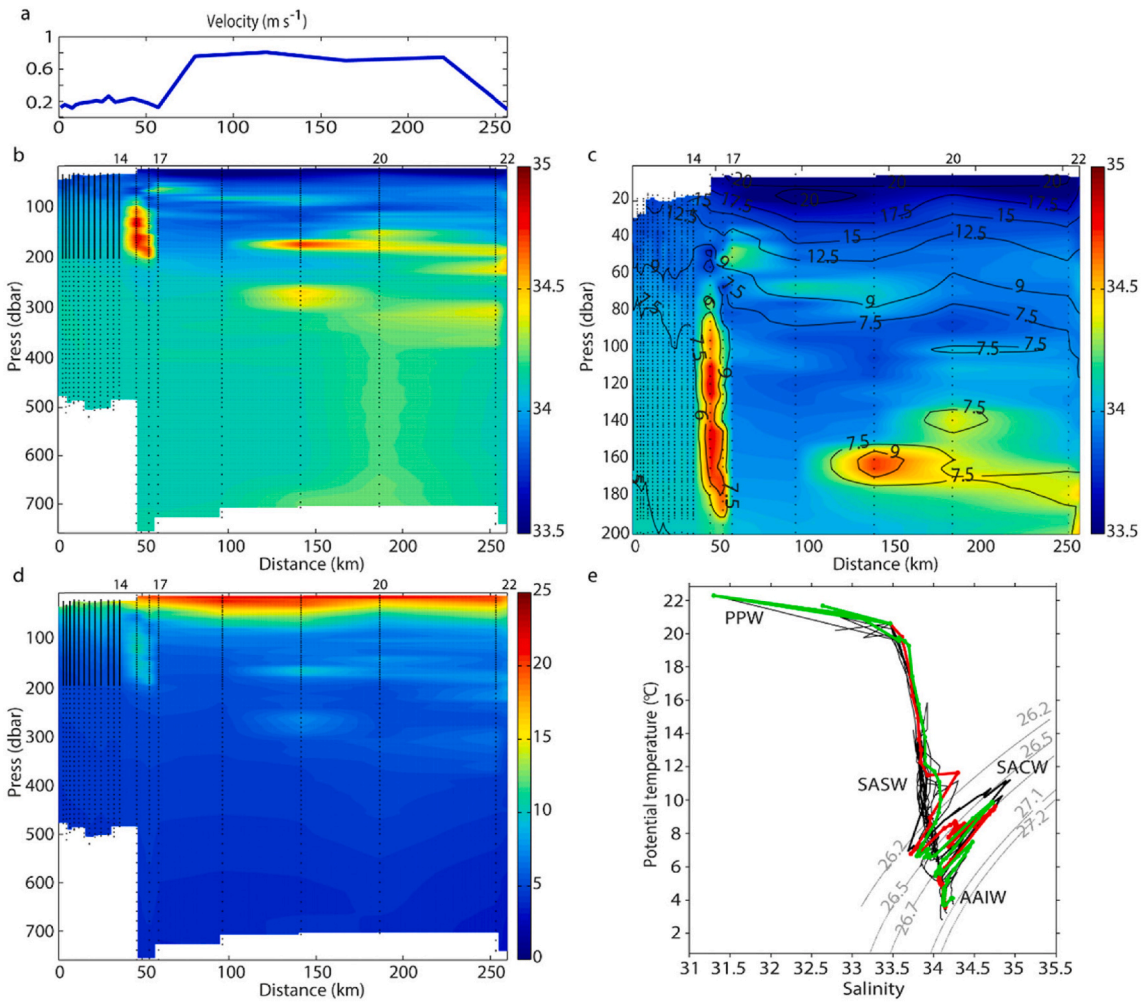

Fig. 9. (a) Velocity of float 9027. Vertical distributions of (b, c) S and (d) θ along the path of float 9027, for the upper (b, d) 740 m and (c) 200 m; the contours in panel c represent isotherms. (e) θ-S diagram for the trajectory of float 9027, profiles 16 and 19 are shown in red and green, respectively.

The position of this off-shelf export is influenced by the location of the BMCF (Combes and Matano, 2018), which explains the large amount of SASW found by Apex-9231, at a position close to both the shelf break and the Confluence point. Besides shelf waters, during the TIC-MOC cruise we also found river origin waters (PPW, $S < 32.5$) as far as 150 km from the shelf-break (Fig. 12b). The CTD cross-frontal sections show how the RdlP plume becomes thinner as it travels east, primarily along the subtropical side of the front (Fig. S4, Supplementary materials). We obtain a similar picture from the GLORYS monthly-mean (March 2015) data: selecting positions along the track of the plume, we observe a 15–20 m thick layer formed by a mixture of PPW and SASW, which extends from the shelf-break to around 300 km (Fig. 12).

We interpret the amount of shelf (SASW) and river (RdlP) water over the BMC region as responding to two different processes. The first one relates to the confluence dynamics, being responsible for the shedding of shallow and swift frontal filaments along the frontal system. The second one responds to the northeasterly winds, inducing offshore surface Ekman transport of the brackish shelf waters. In order to explore these two different dynamical processes, we use a section along the shelf break that spans the entire latitudinal extent of the BMC and where we have both hydrographic and reanalysis data (Fig. 12a). The distribution of density and salinity along this section shows a plume of river-origin waters in the upper 20 m during the time of the cruise, although these brackish waters reach shallower and spread greater in the hydrography than in the reanalysis; the latitudinal extension of isopycnals 23.5 through 24.5 shows that this difference is real, although it is possibly emphasized by the low resolution of the CTD data (Fig. 13). Additionally, the data shows the plume to be ejected on top of the subtropical waters rather than along the surface front, as suggested by the reanalysis (Fig. 4 and Fig. 13 and Fig. S4, Supplementary Material).

In order to explore the influence of the confluence dynamics in the cross-shelf exchanges, we use the reanalysis data to explore if the presence and removal of brackish waters along the shelf-break is related to the amount of PPW water in the BMC. The influence of the river is simply assessed through the mean salinity along the shelf break in the upper 30 m and the amplitude of the shelf-break velocities for brackish waters ($S < 32.5$), while the amount of PPW is computed as the volume of waters in the Confluence region with $S < 32.5$ (Piola et al., 2008a) (Fig. 14). The time series of these three quantities between January and March 2015 reveals a significant (p-value < 0.05) direct Pearson correlation: 0.47 between speed and PPW, −0.21 between salinity and speed, and −0.69 between salinity and PPW, with maximum/minimum speeds and PPW volume corresponding to the time when the water at the shelf-break is freshest/saltiest.

The zero-lag negative correlation between the salinity at the shelf-break and the offshore PPW volume confirms the existence of an intermittent process that swiftly expels surface brackish waters from the shelf along the BMCF. We propose that this mechanism relies on the transient dynamics of the converging boundary currents. Considering that the MC is much faster than the BC, the offshore diversion of the two encountering boundary currents implies the existence of a latitudinal gradient $(\partial/\partial y)$ in the zonal offshore flow u, i.e. $\partial u/\partial y < 0$. If the impinging

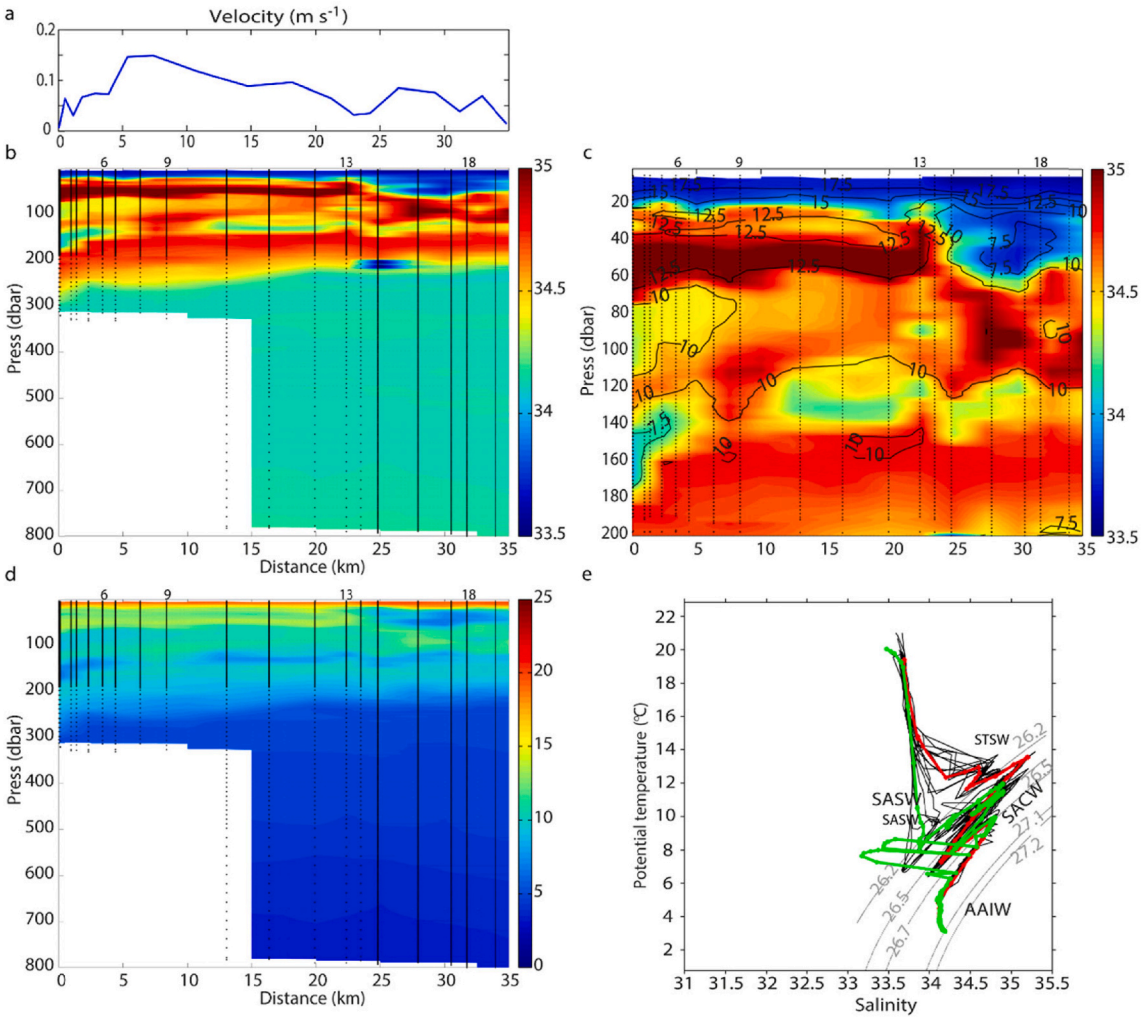

Fig. 10. (a) Velocity of float 9231.Vertical distributions of (b, c) *S* and (d) θ along the path of float 9231, for the upper (a, c) 740 m and (b) 200 m; the contours in panel c represent isotherms. (e) θ-*S* diagram for the trajectory of float 9231, profiles 10 and 15 are shown in red and green, respectively.

currents remained constant, the latitudinal diffusion of momentum between the two offshore-diverting currents would lead to a steady state latitudinal gradient in horizontal flow. However, if the MC accelerates and there is no comparable increase in the BC, the magnitude of the latitudinal gradient will increase, creating a positive vorticity at the shelf break that will drag the shelf waters offshore, along the frontal convergence. The presence of these intermittent filaments of fresh water shows up clearly in the reanalysis, being visible both in snapshots (e.g. for 17 March in Fig. 2d) and in the mean image for the period of the cruise (Fig. 12a). The freshwater transported by these filaments very soon covers a narrow area along the surface BMCF, i.e. at speeds between about 1 and 2 m s^{-1} it would reach between 200 and 500 km offshore in only 2 or 3 days.

The second dynamical process corresponds to the offshore Ekman export of a mixture of river and shelf waters, as already proposed by several authors (Combes and Matano, 2014a, 2018; Guerrero et al., 2014; Matano et al., 2014). These studies have suggested that the presence of PPW in the BMC region is mainly controlled by the along-slope wind regime, with shelf-water being exported during periods of north-easterly winds, directly through Ekman layer transports and indirectly via the creation of a cross-shelf elevation gradient that leads to a geostrophic southwestward flow over the platform.

In order to explore this mechanism, we first calculate the Ekman transport along the shelf-break section between 35.3°S and 40.0°S (Fig. 15a) for the first three months of 2015. During this period the north-easterly winds prevailed, in agreement with the seasonal wind-patterns (Piola et al., 2008), hence favoring the offshore detrainment of surface shelf waters at a rate that exceeded 1Sv during the peak winds, explaining the low along-shelf salinities (Fig. 14) and the widespread RdlP plume (Fig. 13). At the end of the analyzed period, however, there are two reversals in the wind direction (Fig. 16a), which would restrain the off-shelf export of RdlP waters (Fig. 15a) and explain the increase in along-shelf salinity (Fig. 14).

In order to calculate the relation of the off-shelf transport of low-salinity waters and the amount of PPW over the BMC we follow a simple procedure. First, we calculate the accumulated off-shelf Ekman transport (Fig. 15b); we start this summation on January 4 simply because this day is the start of a week of relatively calm winds, which allows assuming that it is a reasonably good time to reset the offshore system. Next, we linearly fit this accumulated offshore transport (Fig. 15b) and calculate the anomaly as the difference between the actual accumulated transport and the linear fit (Fig. 15c). Finally, this anomaly is compared with the water volume over the BMC that has become less dense as a result of the influence of the riverine waters (Fig. 15c). For this purpose, we consider waters lighter than 24.6 kg m^{-3}, which is the upper density level found throughout the along-shelf section (Fig. 13); further, this definition is less restrictive than our earlier PPW definition ($S < 32.5$) and hence considers the possibility of progressive dilution of the riverine waters with the underlying water masses.

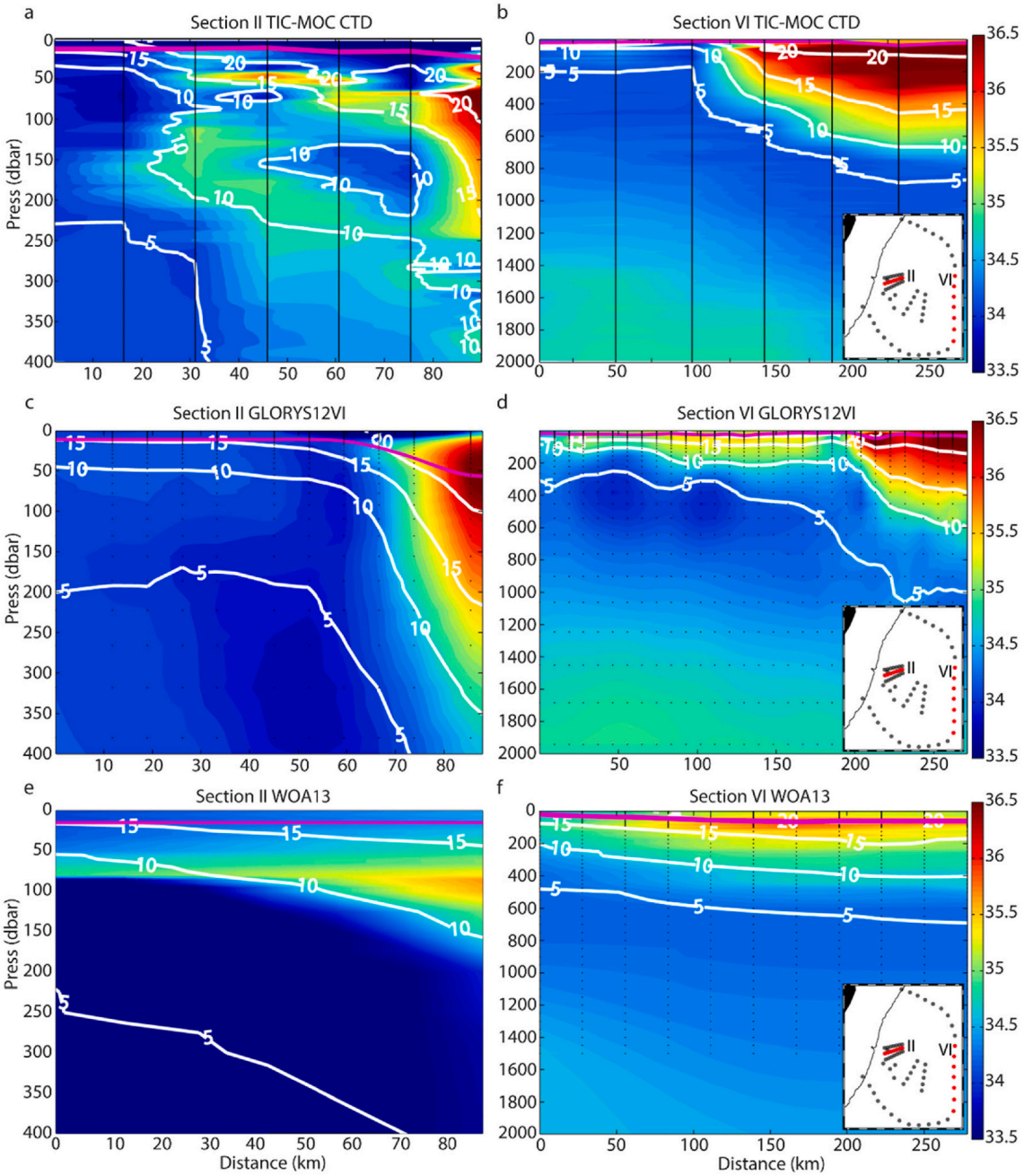

Fig. 11. Vertical sections of salinity S (color-coded), potential temperature θ (white contours) and mixed layer depth (magenta contours) for (a, c, e) section II and (b, d, f) section VI, from (a, b) the CTD casts, (c, d) the GLORYS reanalysis and (e, f) the WOA13 climatology. The black dots locate the stations and measurement depths.

The premise behind these calculations is that the discharge of the RdlP, because of its extremely large drainage basin (over 3 million squared kilometers), changes at relatively slow (seasonal) frequencies (García and Vargas, 1996; Borús and Giacosa, 2014). Hence, the RdlP discharge (mean January–March value of 29,000 $m^3\ s^{-1}$ or about 0.03 Sv) reaches the shelf at a nearly constant rate but it is intermittently exported to the BMC region through the wind pulses. Further, we may assume that the amount of fresh water over the BMC region has some characteristic residence time, which results from the inputs and outputs associated to the major currents and the mesoscale and submesoscale processes. Hence, we assume that the rate of removal of surface waters from the BMC region will be approximately constant, which will cause that for each value of RdlP discharge there is a characteristic PPW volume, i.e. if the river water was transported into the BMC at a constant rate then the volume of PPW over the Confluence would tend to this value; between January and March 2015 the mean PPW volume was 8.4 $\times\ 10^3\ km^3$ (Fig. 15c).

The above calculations also show that the accumulated river discharge (221 km^3 in 88 days; Fig. 15b) is about 4 times less than the amount of surface waters exported from the shelf. This can be interpreted as if the brackish water exported out of the shelf have 1/5 of fresh and 4/5 of salty waters or, assuming that the environment water has a salinity of 35.0, their salinity is about 28.0. Obviously, this water is further salinified through mixing with the salty surface offshore waters over the BMC, leading to the definition of $S < 32.5$ for PPW. This is confirmed by the export associated with the offshore wind pulses, of the order of 100 km^3 (2–3 days exporting 0.4–0.6 Sv, Fig. 15a), which is much less than the average volume of PPW in the region.

The accumulated offshore Ekman transport anomaly and the PPW volume, however, are essentially uncorrelated (Fig. 15c). We may try to

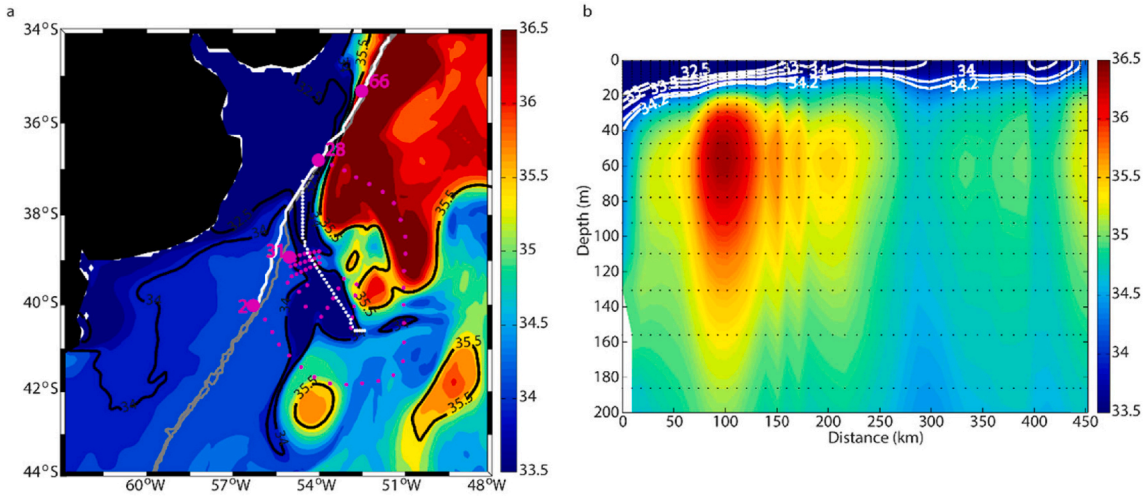

Fig. 12. (a) Mean SSS field during the TIC-MOC cruise, as deduced from the reanalysis. The black contours represent the 32.5, 34.0 and 35.5 isohalines while the grey lines indicate the 200 and 500 m isobaths. The white line shows the section used for computing the cross-shelf Ekman transport (Figs. 15 and 16), the magenta dots are TIC-MOC stations (the large dots indicate those points used for characterizing the along-shelf-break salinity (Fig. 13), and the white dots display the locations along the RdlP plume shown in panel b. (b) Salinity vertical section of the upper 200 m along the RdlP plume, from the shelf-break to the external area of the BMCF, following the model grid points (white dots) in panel a (the black dots locate the stations and measurement depths).

improve the calculation by estimating the amount of actual freshwater in both the cross-shelf Ekman transport and the offshore region. For this purpose, we follow a simple procedure, which considers the mean salinity of the Ekman export transport S_e as compared with the salinity of the unperturbed shelf waters S_s and, similarly, takes into account the salinity of the offshore plume S_p as compared with the salinity of the unperturbed Confluence waters S_c. The salinity of the unperturbed shelf waters is calculated numerically as the mean January–March salinity in the lower half of the reference section along the shelf break, which is assumed to be unaffected by the river plume waters (Figs. 12 and 13), giving $S_s = 34.77$.

Calling T the Ekman transport, which depends solely on the wind and the Coriolis parameter, the associated Ekman transport of freshwater is given by $T(1 - S_e/S_s)$. Similarly, naming V the volume of the offshore plume, the actual offshore volume of freshwater is given by $V(1 - S_p/S_c)$. For our calculations of the time series of S_e and S_p, we set the 24.6 kg m^{-3} isopycnal as the lower limit of both the Ekman offshore transport and the offshore freshwater volume. This selection is based on the density and salinity distributions along the shelf break, which show that this isoneutral can be used as an indicator of both the lower limit of the surface mixed layer and the region of freshwater influence (Fig. 13b). With the above considerations, and setting $S_s = 34.77$ and $S_c = 35.50$, we repeat the above calculations (Fig. 15) but now for freshwater Ekman transport and freshwater offshore volume (Fig. 16). For the January–March period, the peak cross-shelf freshwater transports reach 0.03 Sv (Fig. 16a), which is about the same as the mean RdlP discharge, and the mean freshwater offshore volume is 152 km^3 (Fig. 16c). The time series of the freshwater anomaly cross-shelf transports and off-shelf freshwater volumes are now significantly correlated at zero time-lag (correlation 0.79) (Fig. 16c).

These results suggest that the offshore freshwater volume arises mainly as a consequence of the Confluence dynamics mechanism via offshore stretching filaments but also responds to the surface winds via cross-shelf wind-induced export. Our results show that both mechanisms occur very rapidly (time lag no substantially different from zero). However, we may expect that the narrow and shallow fast-flowing filaments (1–2 m s^{-1}) will stretch the river waters far offshore while the wind-induced Ekman transport in the surface mixed layer (0.1–0.2 m s^{-1}) will accumulate most of the water close to the shelf-break. Considering the mean offshore freshwater volume (152 km^3) and the RdlP mean freshwater discharge for the January–March period (0.03 Sv), we may estimate that the exported shelf waters have a residence time of some 60 days over the Confluence region.

The near and far field cross-frontal sections also suggest that there is a close relation between the 3D frontal structure and the spreading of the low-salinity waters on top of the frontal system. In the near-slope sections the density structure is rather complex (Fig. 3b,d,f), displaying what resembles a double-frontal structure, e.g. in section II the isoneutrals are fairly flat between coordinates 30 and 70 km (Fig. 3b), probably favoring a much greater cross-frontal spreading of the brackish surface waters. In contrast, in the far-field sections there is a sharp frontal system, on top of which we find a thinner filament of low-salinity waters.

4.3. Filament velocities

We expect that the brackish-water filaments are relatively small and highly intermittent, hence far from geostrophic balance. We explore this hypothesis by examining the correlation between brackish waters, identified through their negative salinity anomaly, and the ageostrophic speeds along the frontal jet and the BC (Fig. 17).

We define the (negative) salinity anomaly variable as the absolute value of the difference between the observed salinity and the value it would have according to its temperature in the absence of PPW waters over the BMC region; the PPW-free values correspond to the best-fit curve to the θ-S diagram formed with thermosalinograph and surface CTD data, after excluding salinity values less than 32.5 (Fig. 17b). Further, the ageostrophic surface speed along the ship track is determined as the imbalance between the in-situ VADCP velocity at 200 m depth, which provides the best fit to the altimetry-derived geostrophic velocity, and this surface geostrophic velocity; this is similar to what is done between CTD-derived geostrophic velocity and SADCP velocity (Garzoli and Molinari, 2001; Fu et al., 2017) (Fig. 17c). The largest ageostrophic speeds (>1.0 m s^{-1}) are found along the BCF path, where salinity anomalies are also high (Fig. 17a).

From the salinity anomaly versus ageostrophic speed scatter plot, it is possible to infer a positive correlation (Pearson $r = 0.37$, p-value < 0.001) between both variables (Fig. 17d). It is worth to point out that some of the scattering in this last diagram may partly relate to the low spatiotemporal resolution of altimetry, 15 days and 40 km according to Piola et al. (2013) or 34 days and 100 km according to Ballarotta et al. (2019). Despite so, this significant correlation confirms that the filament

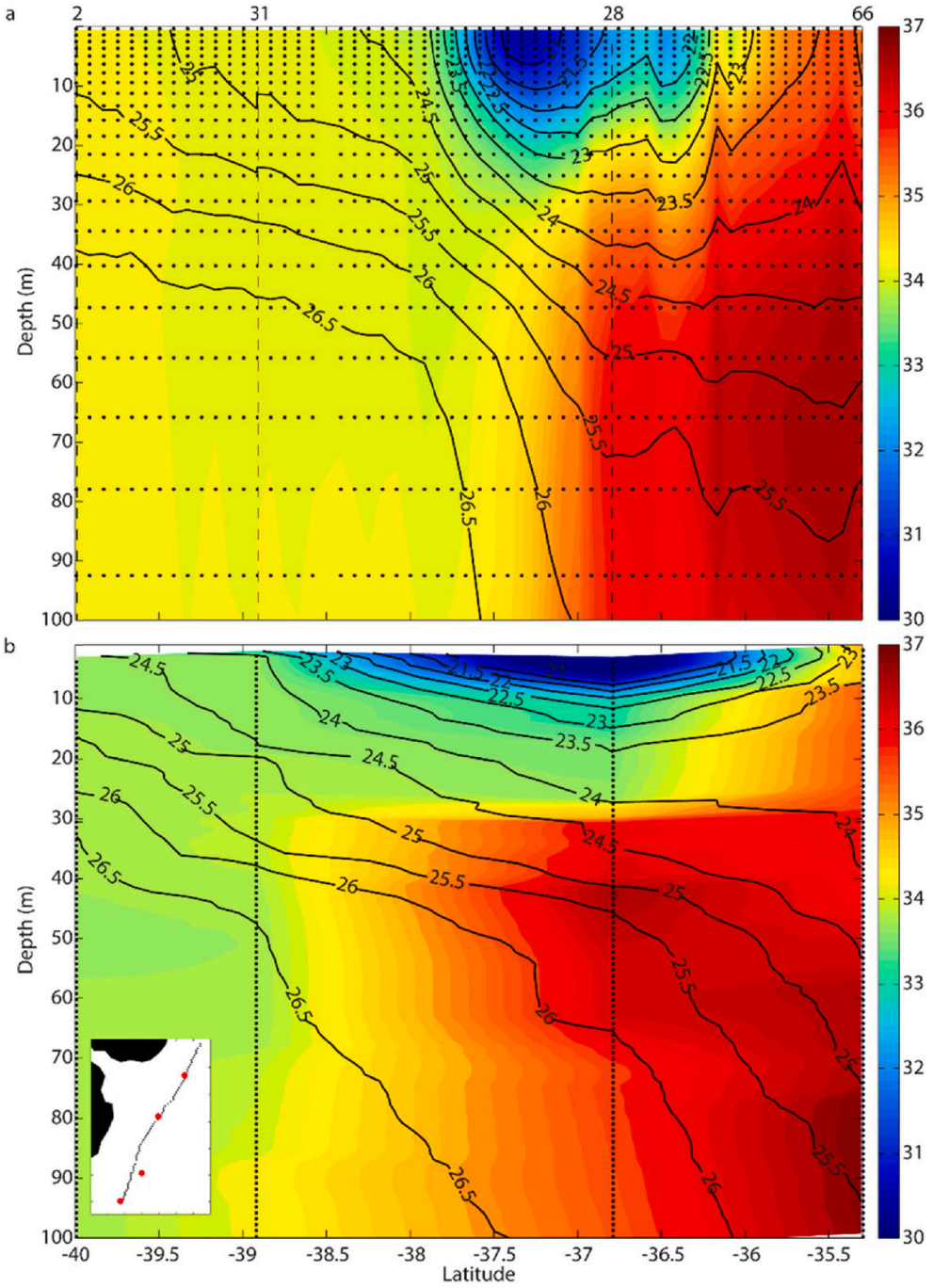

Fig. 13. Vertical sections of the along-shelf-break salinity (color-coded) as derived from (a) the mean March 2015 reanalysis data and (b) the section formed by the CTD stations 2-31-28-66. Neutral density contours (black lines) are at 0.5 kg m^{-3} intervals. The location of the section is shown in the inset of panel b (with the CTD stations as red points) and in Fig. 12a; the black dots locate the stations and measurement depths.

of brackish waters that extends offshore on top de frontal system is indeed largely in ageostrophic balance, therefore explaining the remarkably high observed speeds (peak values up to 2.0 m s^{-1}).

4.4. BMC variability

Up to now, we have mainly presented a stationary picture of the BMC for March 2015. However, this is an extraordinarily variable region, mostly related to the high-frequency migrations of the BCF, as evidenced by its displacements and meandering during the time of the cruise (Fig. 8). Next, by combining the CTD and Apex-9027 profiles, we explore the temporal variability of the thermohaline properties of the upper ocean (down to about 400–500 m) from profiles taken within 2 km or less and time lapses shorter than 5 days (Table 3, Fig. 18). We consider two locations belonging to the near field (CTD49-Apex17 and CTD47-Apex10 pairs) and one location in the far field (CTD61-Apex 22 pair).

The largest thermohaline changes are between CTD49 and Apex17, in the upper 250 m, in a location close and between the BMCF and BCF (Fig. 18a). The CTD49 profile is only 0.7 km to the northeast of Apex17. Nevertheless, during the three days lapse between both casts, the BCF moved significantly to the north (Fig. 8). In this way, the CTD cast ended over the frontal area, leading to the appearance of large (warm-salty) thermohaline subsurface intrusions. In the pair CTD47-Apex10 (Fig. 18b), although the time lapse and distance between both profiles

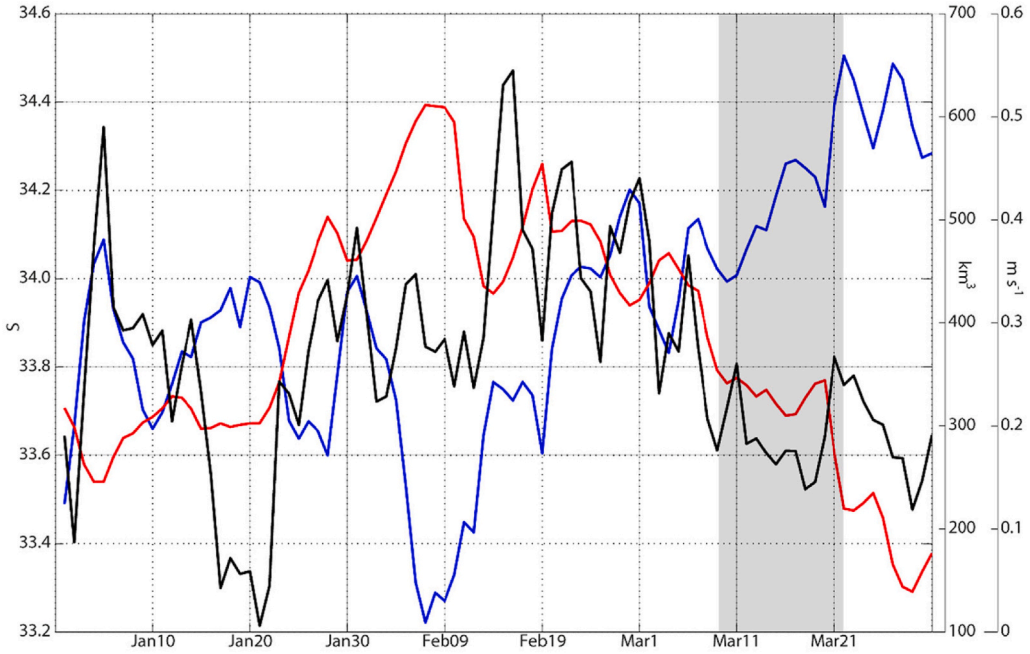

Fig. 14. Along-shelf-break mean salinity in the upper 30 m between 40°S and 35.3°S (blue line, left axis), shelf-break mean speed ($S < 32.5$) (black line, right axis) and the off-shelf PPW volume ($S < 32.5$) as obtained from the GLORYS data (red line, right axis). The location of the along-shelf-break section is illustrated in Fig. 13. The shaded region highlights the TIC-MOC cruise period.

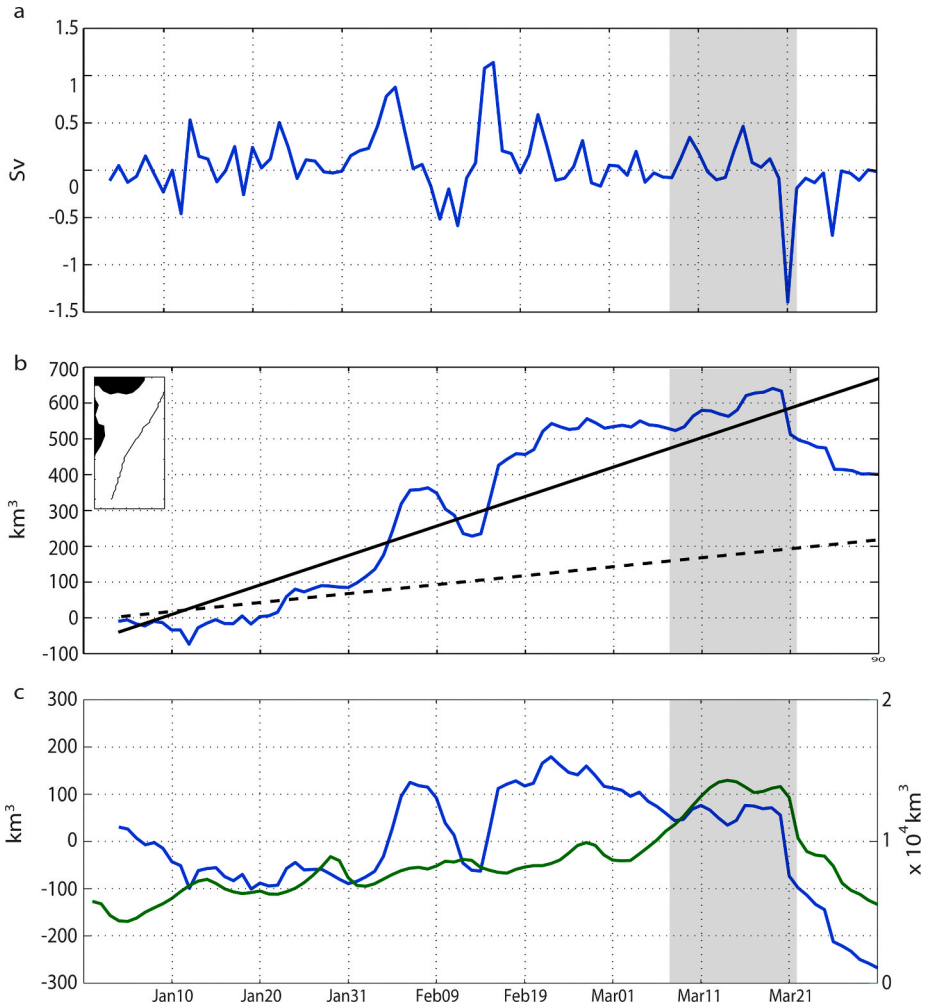

Fig. 15. (a) Wind-induced Ekman transport through the along-shelf-break section (inset in panel b); the negative/positive values indicate transports into/out of the shelf. (b) Cross-shelf accumulated Ekman transport starting on January 4 (blue line) and its linear fit (black line), and accumulated river discharge for this same period (black dashed line). (c) Anomaly of the accumulated cross-shelf Ekman transport (blue line, left axis) determined as the difference between the accumulated cross-shelf Ekman transport and the linear fit in panel b, together with the off-shelf volume above the isoneutral 24.6 kg m^{-3} as obtained from the GLORYS reanalysis (green line, right axis). The shaded region highlights the TIC-MOC cruise period.

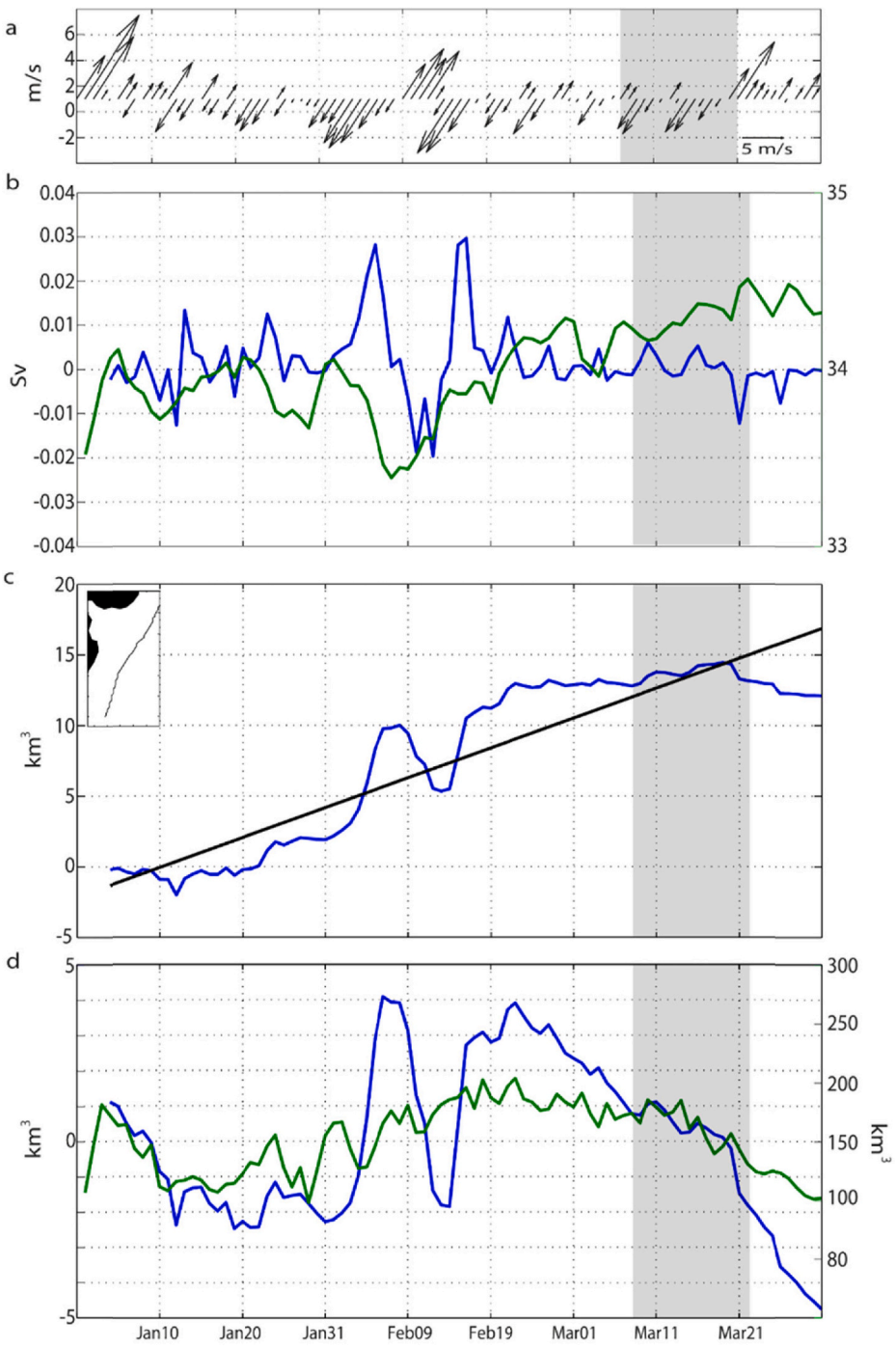

Fig. 16. (a) Mean along-shelf wind vectors in the along-shelf-break section (inset in panel c). (b) Mean salinity of the Ekman export transport S_e (blue line, right vertical axis) and associated freshwater transport (green line, left vertical axis) through the along-shelf-break section; the negative/positive values indicate transports into/out of the shelf. (c) Accumulated cross-shelf freshwater transport (blue line) and its linear fit (black line); the inset shows the location of the along-shelf-break section. (d) Anomaly of the accumulated cross-shelf freshwater transport (blue line, left axis) determined as the difference between the accumulated cross-shelf freshwater transport and the linear fit in panel c, together with the off-shelf freshwater volume above isoneutral 24.6 kg m^{-3} as obtained from GLORYS reanalysis (green line, right axis). The shaded region highlights the TIC-MOC cruise period.

is larger than in the preceding pair, the thermohaline variations are much smaller: both profiles display similar subantarctic θ-S properties, belonging to the inner MC where the thermohaline variability is low and there are no subtropical intrusions (Fig. 9; Orúe-Echevarría et al., 2019c). Finally, the pair in the far field (Apex22-CTD61, Fig. 18c) is located in the border of the SW-AC eddy, separated by 1.4 km and only a few hours apart. Both profiles show the relatively fresh and cold characteristics of the subantarctic waters. As expected from the short-time interval, both casts present similar vertical structure and share the existence of similar thermohaline intrusions.

Thermohaline intrusions were early observed in a high-resolution cross-front section (2–4 km station separation) occupied at around 40°S-53.5°W (Bianchi et al., 2002). Garzoli and Garraffo (1989) suggested that the thermohaline variability depends on the sampling position relative to the BCF. Latitudinal changes in the position of the BCF have been observed at annual and semiannual periods while zonal migrations have been detected at higher frequencies (3–5 months) (Ferrari et al., 2017). Superimposed on these low-frequency motions, shorter spatiotemporal changes can happen in weeks or even days (Legeckis and Gordon, 1982). The displacements and meanders of the BCF also affect the salinity structure of the BMC, especially near the 500-m isobath (Provost and Le Traon, 1993), as is the case for the pair CTD49-Apex17. This situation is most complex when the north-easterly winds over the neighboring continental shelf export river waters. On the other hand, the variability is maximum at the subsurface frontal layers, between 100 and 300 m, particularly in the northern side of the front,

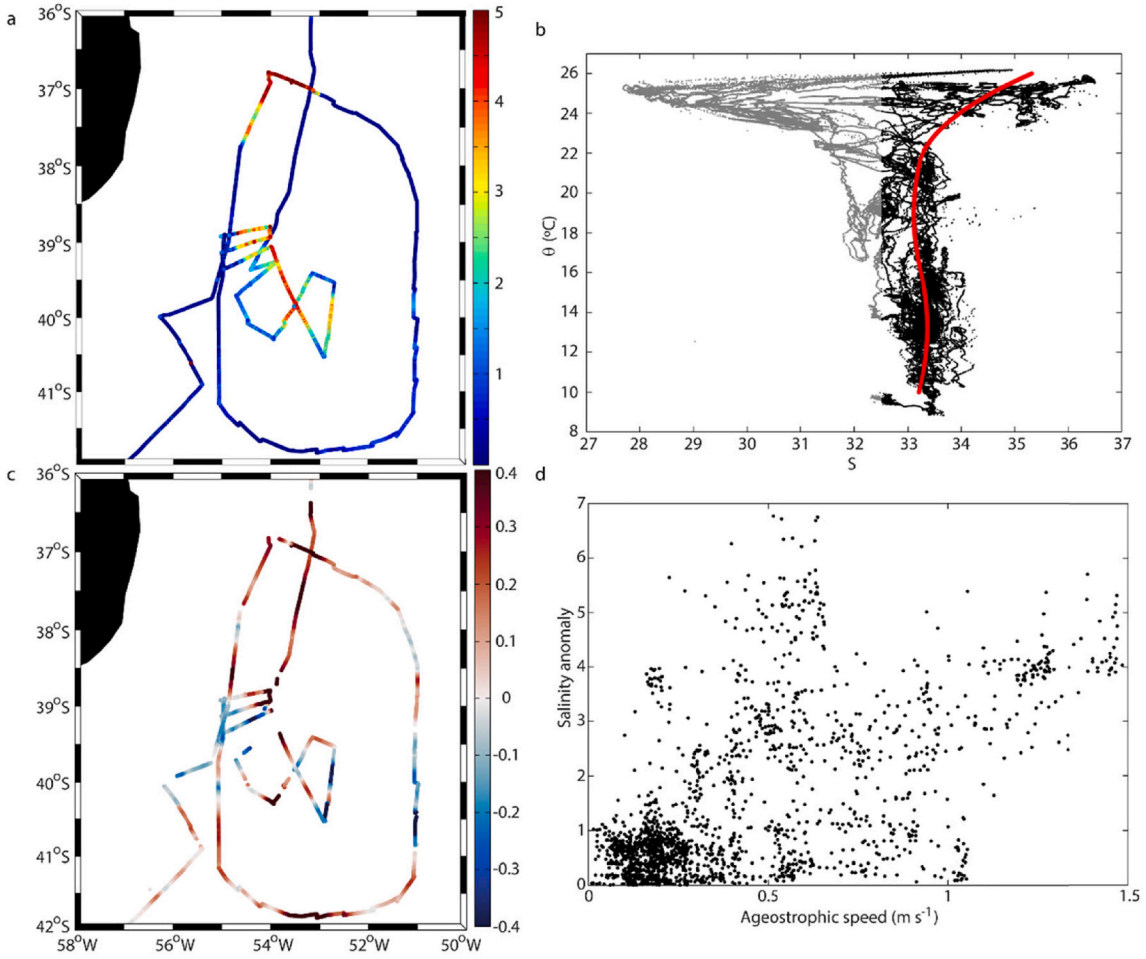

Fig. 17. (a) Surface (negative) salinity anomaly as determined from the thermosalinograph data. (b) θ-S diagram for the thermosalinograph and surface CTD data ($S < 32.5$ grey dots and $S > 32.5$ black dots), including the PPW-free best-fit curve (red line). (c) Ageostrophic surface speed field (m s^{-1}). (d) Salinity anomaly versus ageostrophic speed scatter plot.

Table 3
Pairs of CTD and Apex-9027 profiles used to analyze the temporal variability at the frontal area; the locations and times are indicated, together with the distance between casts.

	Station	Longitude	Latitude	Day	Distance (km)
CTD	49	−54.474	−39.203	2015/03/18	0.7
Apex	17	−54.468	−39.207	2015/03/15	
CTD	47	−54.795	−39.306	2015/03/18	1.9
Apex	10	−54.808	−39.292	2015/03/13	
CTD	61	−52.897	−40.523	2015/03/19	1.4
Apex	22	−52.913	−40.525	2015/03/19	

due to the presence of both mesoscale and submesoscale intrusions (Orúe-Echevarría et al., 2019c).

5. Conclusions

The dataset gathered during the TIC-MOC cruise provides a general hydrographic context of the Brazil-Malvinas Confluence (BMC) for late summer and early fall 2015. This new dataset allows describing the hydrographic and biogeochemical properties in the BMC, a region mostly studied with model or satellite data but rarely with in-situ measurements. We compare these observations with satellite-derived images and reanalysis and climatology data at the time of the cruise. In addition, we analyze the offshore transports of shelf and Rio de la Plata (RdlP) freshwaters into the BMC.

In March 2015, the Malvinas (MC) and Brazil (BC) currents converged at approximately 39.5°S, along the 1000 m isobath, and diverted offshore as a high-velocity frontal jet. The southern position of the BMC over the shelf break responds to its inter-annual variability (Olson et al., 1988; Wainer et al., 2000; Goni and Wainer, 2001). The Subantarctic Front (SAF) only reached 40°S, reflecting the exceptional southern location of the front in 2014–2015 (Ferrari et al., 2017). The confluence of the western boundary currents brought about numerous mesoscale features, the most notorious ones being an intense anticyclonic eddy (SW-AC) centered near 41.0°S-55.0°W and a cyclonic ring (SE-C) with its core at 41.5°S-51.4°W.

The southern margin of the BMC front is dominated by fresh, cold and nutrient-rich subantarctic Malvinas waters, whereas the northern region is depicted by warmer, saltier and nutrient-poor subtropical waters advected within the BC. The frontal region is characterized by an abrupt transition in all sampled properties – potential temperature, salinity, dissolved oxygen, inorganic nutrients. The BMC frontal system is approximately normal to the slope, with the less dense BC waters overriding heavier MC waters; at the front, the subantarctic waters are diverted offshore while simultaneously penetrate northward under the subtropical waters. Both the MC and BC display peak velocities well in excess of 0.6 m s^{-1}, although the intensity of the BC decreases with depth much faster than the MC. The two boundary currents converge into the BMC front where the surface waters flow eastward at high speed, up to 2.0 m s^{-1}, far from geostrophic balance.

On top of the BMC, there is a large amount of relatively fresh shelf

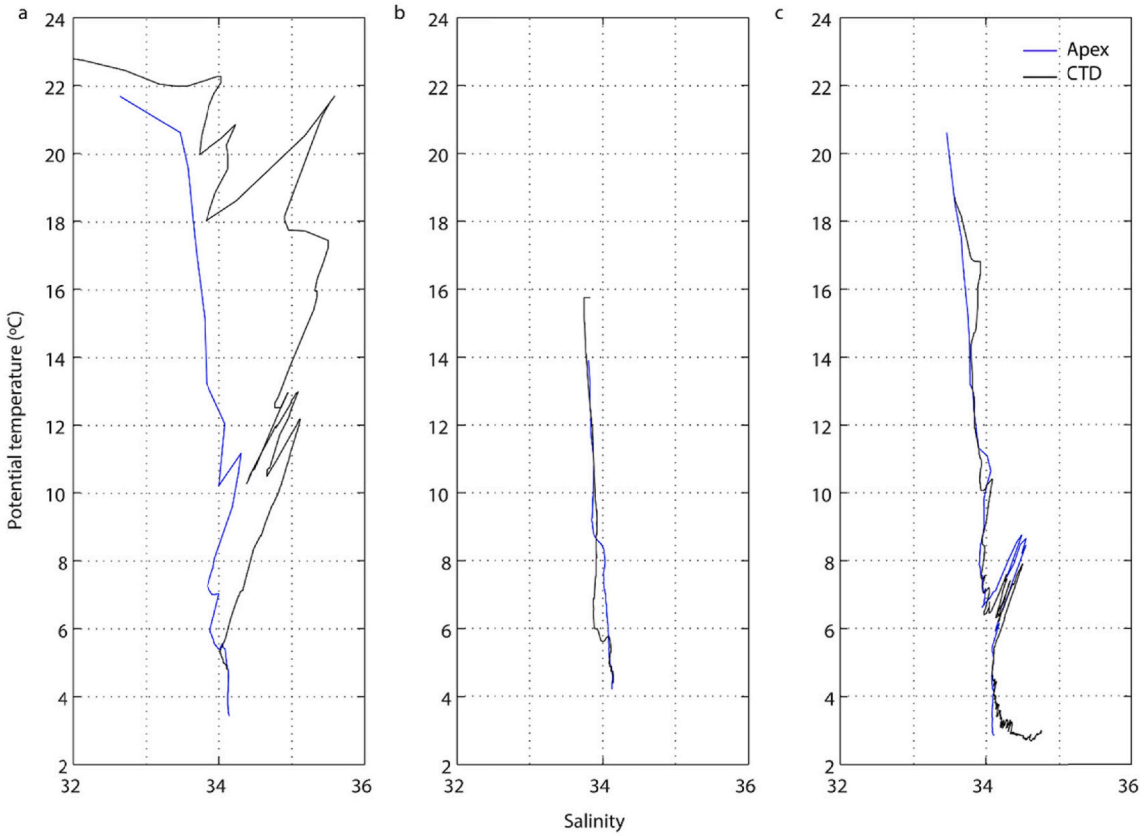

Fig. 18. Comparison of θ-S diagrams among the closest CTD (black) and Apex-9027 (blue) stations: (a) CTD49-Apex17, (b) CTD47-Apex10, and (c) CTD61-Apex22, corresponding to the three pairs in Table 3.

water, which responds to offshore stretching filaments and wind-induced cross-shelf transports. We propose that these brackish filaments are swiftly driven by the offshore dynamics of the meeting boundary currents, as reflected by the zero lag-time between both water speed and salinity at the shelf break and the offshore volume of plume water. Similarly, the wind-induced offshore transport of shelf waters also acts rapidly, as shown by the zero lag-time between the Ekman cross-shelf freshwater transport and the amount of freshwater in the Confluence region; however, we may expect that wind-induced export will initially pile up the brackish waters much closer to the shelf break than the filaments. Both processes appear to be significant in the offshore transport of brackish waters in the Confluence region.

Overall, the regional and mesoscale fields are well captured by the satellite images, notably the ADT images, and the eddy-resolving Mercator reanalysis. In particular, the SSS reanalysis indicates that a plume of brackish and cold waters stretched out as a convoluted shallow filament over the frontal region, in agreement with observations. However, the frontal system in the reanalysis is positioned further north than observed, about 100 km in the far offshore sections and several times more in the nearshore sections. Additionally, the reanalysis is unable to reproduce the complex vertical structure of the frontal system, as revealed by the CTD vertical sections and profiling floats. A highly-distorted double front appears near the continental slope, with thermohaline intrusions on both sides of the front, in contrast with a much sharper and steeper shape several hundred kilometers from the slope.

The BMC shows up as a very complex region, representing not only the meeting point of subantarctic and tropical waters but also the locus of substantial water export from the shelf to the deep ocean. These different water masses converge and mix in the BMC, the subantarctic waters also subduct under the subtropical ones, and they all are exported offshore following intricate horizontal patterns. Our results confirm that the models and reanalysis are capable of capturing the major features but certainly fail at representing the details, especially the subsurface processes. Additional observations and a better understanding of those processes leading to vertical motions and submesoscale mixing in frontal regions is yet necessary for achieving realistic forecasts.

Declaration of competing interest

The authors declare that they have no known competing financial interests or personal relationships that could have appeared to influence the work reported in this paper.

Acknowledgments

We would like to thank the crew and technicians of the R/V Hespérides for their support and indispensable help during the TIC-MOC cruise. We also thank the journal's editor and our two reviewers for providing constructive comments that helped improve the final version of this manuscript. We acknowledge support from the Spanish Government through grants CTM2011-28867 (TIC-MOC project), CTM2014-56987-P (VA-DE-RETRO project) and RTI2018-100844-B-C33 (SAGA project), and through the funding of PhD scholarships for D.O.E. (FPU2013-02884), C.H. (CSIC JAE-Predoc program), S.R.G. (BES-2012-055970) and I.V.C. (BES-2015-071314). We also recognize the institutional support of the Spanish Government through the Severo Ochoa Centre of Excellence accreditation (CEX2019-000928-S).

Appendix A. Supplementary data

Supplementary data to this article can be found online at https://doi.org/10.1016/j.dsr.2021.103533.

References

Acha, E.M., Mianzan, H.W., Guerrero, R.A., Favero, M., Bava, J., 2004. Marine fronts at the continental shelves of austral South America: physical and ecological processes. J. Mar. Syst. 44 (1), 83–105. https://doi.org/10.1016/j.jmarsys.2003.09.005.

Artana, C., Ferrari, R., Koenig, Z., Sennéchael, N., Saraceno, M., Piola, A.R., Provost, C., 2018. Malvinas Current volume transport at 41°S: a 24 yearlong time series consistent with mooring data from 3 decades and satellite altimetry. J. Geophys. Res.: Oceans 123, 378–398. https://doi.org/10.1002/2017JC013600.

Artana, C., Lellouche, J.M., Park, Y.H., Garric, G., Koenig, Z., Sennéchael, N., Ferrari, R., Piola, A.R., Saraceno, M., Provost, C., 2018b. Fronts of the Malvinas Current System: surface and subsurface expressions revealed by satellite altimetry, Argo floats, and Mercator operational model outputs. J. Geophys. Res.: Oceans 123, 5261–5285. https://doi.org/10.1029/2018JC013887.

Artana, C., Provost, C., Lellouche, J.-M., Rio, M.-H., Ferrari, R., Sennéchael, N., 2019. The Malvinas current at the confluence with the Brazil current: inferences from 25 years of Mercator Ocean reanalysis. J. Geophys. Res.: Oceans 124, 7178–7200. https://doi.org/10.1029/2019JC015289.

Assireu, A.T., Stevenson, M.R., Stech, J.L., 2003. Surface circulation and kinetic energy in the SW Atlantic obtained by drifters. Continent. Shelf Res. 23, 145–157. https://doi.org/10.1016/S0278-4343(02)00190-5.

Atlas, R., Hoffman, R.N., Ardizzone, J., Leidner, S.M., Jusem, J.C., Smith, D.K., Gombos, D., 2011. A cross-calibrated, multiplatform ocean surface wind velocity product for meteorological and oceanographic applications. Bull. Am. Meteorol. Soc. 92 (2), 157–174. https://doi.org/10.1175/2010BAMS2946.1.

Ballarotta, M., Ubelmann, C., Pujol, M.-I., Taburet, G., Fournier, F., Legeais, J.-F., Faugère, Y., Delepoulle, A., Chelton, D., Dibarboure, G., Picot, N., 2019. On the resolutions of ocean altimetry maps. Ocean Sci. 15, 1091–1109. https://doi.org/10.5194/os-15-1091-2019.

Barré, N., Provost, C., Saraceno, M., 2006. Spatial and temporal scales of the Brazil–Malvinas Current confluence documented by simultaneous MODIS Aqua 1.1-km resolution SST and color images. Adv. Space Res. 37 (4), 770–786. https://doi.org/10.1016/j.asr.2005.09.026.

Berden, G., Charo, M., Möller, O.O., Piola, A.R., 2020. Circulation and hydrography in the western south atlantic shelf and export to the deep adjacent ocean: 30°S to 40°S. J. Geophys. Res.: Oceans 125, e2020JC016500. https://doi.org/10.1029/2020JC016500.

Bianchi, A.A., Giulivi, C.F., Piola, A.R., 1993. Mixing in the Brazil-Malvinas confluence. Deep Sea Res. Oceanogr. Res. Pap. 40 (7), 1345–1358. https://doi.org/10.1016/0967-0637(93)90115-J.

Bianchi, A.A., Pino, D.R., Perlender, H.G.I., Osiroff, A.P., Segura, V., Lutz, V., Clara, M.L., Balestrini, C.F., Piola, A.R., 2009. Annual balance and seasonal variability of sea-air CO2 fluxes in the Patagonia Sea: their relationship with fronts and chlorophyll distribution. J. Geophys. Res.: Oceans 114, C03018. https://doi.org/10.1029/2008JC004854.

Bianchi, A.A., Piola, A.R., Collino, G.J., 2002. Evidence of double diffusion in the Brazil–Malvinas Confluence. Deep Sea Res. Oceanogr. Res. Pap. 49 (1), 41–52. https://doi.org/10.1016/S0967-0637(01)00039-5.

Borús, J., Giacosa, J., 2014. Evaluación de caudales diarios descargados por los grandes ríos del sistema del plata al río de la plata. Dirección de Sistemas de Información y Alerta Hidrológico Instituto Nacional del Agua, Ezeiza, Argentina, 2014.

Bower, A., Lozier, S., Biastoch, A., Drouin, K., Foukal, N., Furey, H., Lankhorst, M., Rühs, S., Zou, S., 2019. Lagrangian views of the pathways of the atlantic meridional overturning circulation. J. Geophys. Res.: Oceans 124 (8), 5313–5335. https://doi.org/10.1029/2019JC015014.

Carranza, M.M., Gille, S.T., Piola, A.R., Charo, M., Romero, S.I., 2017. Wind modulation of upwelling at the shelf-break front off Patagonia: observational evidence. J. Geophys. Res.: Oceans 122 (3), 2401. https://doi.org/10.1002/2016JC012059, 242.

Combes, V., Matano, R.P., 2014a. Trends in the Brazil/Malvinas confluence region. Geophys. Res. Lett. 41 (24), 8971–8977. https://doi.org/10.1002/2014GL062523.

Combes, V., Matano, R.P., 2014b. A two-way nested simulation of the oceanic circulation in the Southwestern Atlantic. J. Geophys. Res.: Oceans 119 (2), 731–756. https://doi.org/10.1002/2016JC012059.

Combes, V., Matano, R.P., 2018. The Patagonian shelf circulation: drivers and variability. Prog. Oceanogr. 167, 24–43. https://doi.org/10.1016/j.pocean.2018.07.003.

Confluence Group, Confluence 1988-1990, 1990. An intensive study of the Southwestern Atlantic. Eos Trans. AGU 71 (41), 1131–1134. https://doi.org/10.1029/90EO00313.

Dogliotti, A.I., Lutz, V.A., Segura, V., 2014. Estimation of primary production in the southern Argentine continental shelf and shelf-break regions using field and remote sensing data. Rem. Sens. Environ. 140, 497–508. https://doi.org/10.1016/j.rse.2013.09.021.

Ferrari, R., Artana, C., Saraceno, M., Piola, A.R., Provost, C., 2017. Satellite altimetry and current-meter velocities in the Malvinas current at 41°S: comparisons and modes of variations. J. Geophys. Res.: Oceans 122 (12), 9572–9590. https://doi.org/10.1002/2017JC013340.

Fetter, A.F.H., Matano, R.P., 2008. On the origins of the variability of the Malvinas Current in a global, eddy-permitting numerical simulation. J. Geophys. Res.: Oceans 113, C11018. https://doi.org/10.1029/2008JC004875.

Firing, E., 1995. Processing ADCP Data with the CODAS Software System Version 3.1. Joint Institute for Marine and Atmospheric Research, University of Hawaii & National Oceanographic Data Center, Bremerhaven, PANGAEA.

Franco, B.C., Palma, E.D., Combes, V., Acha, E.M., Saraceno, M., 2018. Modeling the offshore export of subantarctic shelf waters from the patagonian shelf. J. Geophys. Res.: Oceans 123, 4491–4502. https://doi.org/10.1029/2018JC013824.

Fu, Y., Karstensen, J., Brandt, P., 2017. On the meridional ageostrophic transport in the tropical Atlantic. Ocean Sci. 13, 531–549. https://doi.org/10.5194/os-13-531-2017.

Garcia, C.A.E., Sarma, Y.V.B., Mata, M.M., Garcia, V.M.T., 2004. Chlorophyll variability and eddies in the Brazil–Malvinas Confluence region. Deep Sea Res. Part II Top. Stud. Oceanogr. 51 (1), 159–172. https://doi.org/10.1016/j.dsr2.2003.07.016.

García, N.O., Vargas, W.M., 1996. The spatial variability of runoff and precipitation in the Rio de la Plata basin. Hydrol. Sci. J. 41 (3), 279–299.

Garzoli, S.L., 1993. Geostrophic velocity and transport variability in the Brazil-Malvinas Confluence. Deep Sea Res. Oceanogr. Res. Pap. 40 (7), 1379–1403. https://doi.org/10.1016/0967-0637(93)90118-M.

Garzoli, S.L., Bianchi, A., 1987. Time-space variability of the local dynamics of the Malvinas-Brazil confluence as revealed by inverted echo sounders. J. Geophys. Res.: Oceans 92 (C2), 1914–1922. https://doi.org/10.1029/JC092iC02p01914.

Garzoli, S.L., Garraffo, Z., 1989. Transports, frontal motions and eddies at the Brazil-Malvinas currents confluence. Deep Sea Research Part A. Oceanographic Research Papers 36 (5), 681–703. https://doi.org/10.1016/0198-0149(89)90145-3.

Garzoli, S.L., Gordon, A.L., 1996. Origins and variability of the benguela current. J. Geophys. Res.: Oceans 101 (C1), 897–906. https://doi.org/10.1029/95JC03221.

Garzoli, S.L., Matano, R., 2011. the South atlantic and the atlantic meridional overturning circulation. Deep Sea Res. Part II Top. Stud. Oceanogr. 58 (17), 1837–1847. https://doi.org/10.1016/j.dsr2.2010.10.063.

Garzoli, S.L., Molinari, R.L., 2001. Ageostrophic transport in the upper layers of the tropical Atlantic Ocean. Geophys. Res. Lett. 28, 4619–4622. https://doi.org/10.1029/2001GL013473.

Gaube, P., McGillicuddy Jr., D.J., Chelton, D.B., Behrenfeld, M.J., Strutton, P.G., 2014. Regional variations in the influence of mesoscale eddies on near-surface chlorophyll. J. Geophys. Res.: Oceans 119 (12), 8195–8220. https://doi.org/10.1002/2014JC010111.

Goni, G., Kamholz, S., Garzoli, S., Olson, D., 1996. Dynamics of the Brazil-Malvinas Confluence based on inverted echo sounders and altimetry. J. Geophys. Res.: Oceans 101 (C7), 16273–16289. https://doi.org/10.1029/96JC01146.

Goni, G.J., Wainer, I., 2001. Investigation of the Brazil Current front variability from altimeter data. J. Geophys. Res.: Oceans 106 (C12), 31117–31128. https://doi.org/10.1029/2000JC000396.

Gordon, A.L., 1981. South Atlantic thermocline ventilation. Deep sea research Part A. Oceanographic Research Papers 28 (11), 1239–1264. https://doi.org/10.1016/0198-0149(81)90033-9.

Gordon, A.L., 1989. Brazil-Malvinas confluence–1984. Deep sea research Part A. Oceanographic Research Papers 36 (3), 359–384. https://doi.org/10.1016/0198-0149(89)90042-3.

Gordon, A.L., Greengrove, C.L., 1986. Geostrophic circulation of the Brazil-falkland confluence. Deep sea research Part A. Oceanographic Research Papers 33 (5), 573–585. https://doi.org/10.1016/0198-0149(86)90054-3.

Guerrero, R.A., Piola, A.R., 1997. Masas de agua en la plataforma continental. El mar Argentino y sus Recursos Pesqueros, 1E. E. Boschi, 107–118. Instituto Nacional de Investigación y Desarrollo Pesquero, Mar del Plata, Argentina, 1997.

Guerrero, R.A., Piola, A.R., Fenco, H., Matano, R.P., Combes, V., Chao, Y., James, C., Palma, E.D., Saraceno, M., Strub, P.T., 2014. The salinity signature of the cross-shelf exchanges in the Southwestern Atlantic Ocean: Satellite observations. Geophys. Res. Lett. Oceans 119, 7794–7810. https://doi.org/10.1002/2014JC010113.

Jullion, L., Heywood, K.J., NaveiraGarabato, A.C., Stevens, D.P., 2010. Circulation and water mass modification in the Brazil–Malvinas confluence. J. Phys. Oceanogr. 40 (5), 845–864. https://doi.org/10.1175/2009JPO4174.1.

Kahl, L.C., Bianchi, A.A., Osiroff, A.P., Pino, D.R., Piola, A.R., 2017. Distribution of sea-air CO2 fluxes in the Patagonian Sea: seasonal, biological and thermal effects. Continent. Shelf Res. 143, 18–28. https://doi.org/10.1016/j.csr.2017.05.011.

Legeckis, R., Gordon, A.L., 1982. Satellite observations of the Brazil and falkland currents— 1975 1976 and 1978. Deep sea research Part A. Oceanographic Research Papers 29 (3), 375–401. https://doi.org/10.1016/0198-0149(82)90101-7.

Lentini, C.A.D., Goni, G.J., Olson, D.B., 2006. Investigation of Brazil Current rings in the confluence region. J. Geophys. Res.: Oceans 111 (C6). https://doi.org/10.1029/2005JC002988.

Locarnini, R.A., Mishonov, A.V., Antonov, J.I., Boye, T.P., Garcia, H.E., Baranova, O.K., Seidov, D., 2013. world ocean Atlas 2013, volume 1: temperature. In: Levitus, S., Mishonov Technical, A. (Eds.), NOAA Atlas NESDIS, vol. 73, p. 40.

Lumpkin, R., Garzoli, S., 2011. Interannual to decadal changes in the western South Atlantic's surface circulation. J. Geophys. Res.: Oceans 116 (C1). https://doi.org/10.1029/2010JC006285.

Maamaatuaiahutapu, K., Garçon, V., Provost, C., Mercier, H., 1998. Transports of the Brazil and Malvinas currents at their confluence. J. Mar. Res. 56 (2), 417–438. https://doi.org/10.1357/002224098321822366.

Maamaatuaiahutapu, K., Garçon, V.C., Provost, C., Boulahdid, M., Bianchi, A.A., 1994. Spring and winter water mass composition in the Brazil-Malvinas Confluence. J. Mar. Res. 52 (3), 397–426. https://doi.org/10.1357/0022240943077064.

Maamaatuaiahutapu, K., Garçon, V.C., Provost, C., Boulahdid, M., Osiroff, A.P., 1992. Brazil-Malvinas Confluence: water mass composition. J. Geophys. Res.: Oceans 97 (C6), 9493–9505. https://doi.org/10.1029/92JC00484.

Mason, E., Pascual, A., Gaube, P., Ruiz, S., Pelegrí, J.L., Delepoulle, A., 2017. Subregional characterization of mesoscale eddies across the Brazil-Malvinas Confluence. J. Geophys. Res.: Oceans 122 (4), 3329–3357. https://doi.org/10.1002/2016JC012611.

Matano, R.P., 1993. On the separation of the Brazil current from the coast. J. Phys. Oceanogr. 23 (1), 79–90. https://doi.org/10.1175/1520-0485(1993)023<0079:OTSOTB>2.0.CO;2.

Matano, R.P., Combes, V., Piola, A.R., Guerrero, R., Palma, E.D., Strub, P.T., James, C., Fenco, H., Chao, Y., Saraceno, M., 2014. The salinity signature of the cross-shelf

exchanges in the Southwestern Atlantic Ocean: numerical simulations. J. Geophys. Res.: Oceans 119 (11), 7949–7968. https://doi.org/10.1002/2014JC010116.
Matano, R.P., Palma, E.D., Piola, A.R., 2010. The influence of the Brazil and Malvinas currents on the southwestern atlantic shelf circulation. Ocean Sci. 6 (4), 983–995. https://doi.org/10.5194/os-6-983-2010.
McCartney, M.S., 1977. Subantarctic mode water. A voyage of Discovery. Deep-Sea Res. 24, 103–119, 1977.
McCartney, M.S., 1982. The subtropical recirculation of Mode Waters. J. Mar. Res. 40 (Suppl. l), 427–464.
Meinen, C.S., Garzoli, S.L., Perez, R.C., Campos, E., Piola, A.R., Chidichimo, M.P., Dong, S., Sato, O.T., 2017. Characteristics and causes of deep western boundary current transport variability at 34.5° S during 2009–2014. Ocean Sci. 13 (1), 175–194. https://doi.org/10.5194/os-13-175-2017.
Meinen, C.S., Piola, A.R., Perez, R.C., Garzoli, S.L., 2012. Deep Western Boundary Current transport variability in the South Atlantic: preliminary results from a pilot array at 34.5° S. Ocean Sci. 8 (6), 1041–1054. https://doi.org/10.5194/os-8-1041-2012.
Meinen, C.S., Speich, S., Perez, R.C., Dong, S., Piola, A.R., Garzoli, S.L., Baringer, M.O., Gladyshev, S., Campos, E.J.D., 2013. Temporal variability of the meridional overturning circulation at 34.5°S: results from two pilot boundary arrays in the South Atlantic. J. Geophys. Res.: Oceans 118 (12), 6461–6478. https://doi.org/10.1002/2013JC009228.
Meinen, C.S., Speich, S., Piola, A.R., Ansorge, I., Campos, E., Kersalé, M., Terre, T., Chidichimo, M.P., Lamont, T., Sato, O.T., Perez, R.C., Valla, D., Berg, M., Le Hénaff, M., Dong, S., Garzoli, S.L., 2018. Meridional overturning circulation transport variability at 34.5°S during 2009–2017: baroclinic and barotropic flows and the dueling influence of the boundaries. Geophys. Res. Lett. 45 (9), 4180–4188. https://doi.org/10.1029/2018GL077408.
Molinelli, E., 1978. Isohaline thermoclines in the southeast pacific ocean. J. Phys. Oceanogr. 8 (6), 1139–1145. https://doi.org/10.1175/1520-0485(1978)008<1139:ITITSP>2.0.CO;2.
Möller, O.O., Piola, A.R., Freitas, A.C., Campos, E.J.D., 2008. The effects of river discharge and seasonal winds on the shelf off southeastern South America. Continent. Shelf Res. 28 (13), 1607–1624. https://doi.org/10.1016/j.csr.2008.03.012.
Oliveira, L.R., Piola, A.R., Mata, M.M., Soares, I.D., 2009. Brazil Current surface circulation and energetics observed from drifting buoys. J. Geophys. Res. 114, C10006. https://doi.org/10.1029/2008JC004900.
Olson, D.B., Podestá, G.P., Evans, R.H., Brown, O.B., 1988. Temporal variations in the separation of Brazil and Malvinas currents. Deep sea research Part A. Oceanographic Research Papers 35 (12), 1971–1990. https://doi.org/10.1016/0198-0149(88)90120-3.
Orsi, A.H., Whitworth, T., Nowlin, W.D., 1995. On the meridional extent and fronts of the Antarctic Circumpolar Current. Deep Sea Res. Oceanogr. Res. Pap. 42 (5), 641–673. https://doi.org/10.1016/0967-0637(95)00021-W.
Orúe-Echevarría, D., Pelegrí, J.L., Alonso-González, I.J., Benítez-Barrios, V.M., De La Fuente, P., Emelianov, M., Gasser, M., Herrero, C., Isern-Fontanet, J., Peña-Izquierdo, J., Ramírez-Garrido, S., Rosell-Fieschi, M., Salvador, J., Saraceno, M., Valla, D., Vidal, M., 2019a. Dataset on the TIC-MOC cruise onboard the R/V Hespérides, March 2015, Brazil-Malvinas confluence. Data in Brief 22, 185–194. https://doi.org/10.1016/j.dib.2018.12.004.
Orúe-Echevarría, D., Pelegrí, J.L., Machín, F., Hernández-Guerra, A., Emelianov, M., 2019b. Inverse modeling the Brazil-Malvinas confluence. J. Geophys. Res.: Oceans 124. https://doi.org/10.1029/2018JC014733.
Orúe-Echevarría, D., Castellanos, P., Sans, J., Emelianov, M., Vallès-Casanova, I., Pelegrí, J.L., 2019c. Temperature spatiotemporal correlation scales in the Brazil-Malvinas Confluence from high-resolution in situ and remote sensing data. Geophys. Res. Lett. 46, 13234–13243. https://doi.org/10.1029/2019GL084246.
Palma, E.D., Matano, R.P., Piola, A.R., 2004. A numerical study of the Southwestern Atlantic Shelf circulation: barotropic response to tidal and wind forcing. J. Geophys. Res.: Oceans 109 (C8). https://doi.org/10.1029/2004JC002315.
Palma, E.D., Matano, R.P., Piola, A.R., 2008. A numerical study of the Southwestern Atlantic Shelf circulation: stratified ocean response to local and offshore forcing. J. Geophys. Res.: Oceans 113 (C11). https://doi.org/10.1029/2007JC004720.
Palter, J.B., Sarmiento, J.L., Gnanadesikan, A., Simeon, J., Slater, R.D., 2010. Fueling export production: nutrient return pathways from the deep ocean and their dependence on the Meridional Overturning Circulation. Biogeosciences 7 (11), 3549–3568. https://doi.org/10.5194/bg-7-3549-2010.
Paniagua, G.F., Saraceno, M., Piola, A.R., Guerrero, R., Provost, C., Ferrari, R., Lago, S.L., Artana, C.I., 2018. Malvinas current at 40°–41°S: first assessment of temperature and salinity temporal variability. J. Geophys. Res.: Oceans 123 (8), 5323–5340. https://doi.org/10.1029/2017JC013666.
Pelegrí, J.L., Orúe-Echevarría, D., Alonso-González, I.J., Benítez-Barrios, V.M., De La Fuente, P., Emelianov, M., et al., 2018. Data for the March 2015 TIC-MOC Cruise, R/V Hespérides, Brazil-Malvinas Confluence. Mendeley data. https://doi.org/10.17632/hk8t43z3t3.2.
Peterson, R.G., 1992. The boundary currents in the western Argentine Basin. Deep Sea Research Part A. Oceanographic Research Papers 39 (3), 623–644. https://doi.org/10.1016/0198-0149(92)90092-8.
Peterson, R.G., Whitworth, T., 1989. The subantarctic and polar fronts in relation to deep water masses through the southwestern Atlantic. J. Geophys. Res.: Oceans 94 (C8), 10817–10838. https://doi.org/10.1029/JC094iC08p10817.
Piola, A.R., Matano, R., 2001. Brazil and falklands (Malvinas) currents. In: Steele, J.H., Turekian, K.K., Thorpe, S.A. (Eds.), Encyclopedia of Ocean Sciences. Acad. Press, London, pp. 340–349. https://doi.org/10.1006/rwos.2001.0358.
Piola, A.R., Campos, E.J.D., Möller, O.O., Charo, M., Martinez, C., 2000. Subtropical shelf front off eastern South America. J. Geophys. Res.: Oceans 105 (C3), 6565–6578. https://doi.org/10.1029/1999JC000300.
Piola, A.R., Franco, B.C., Palma, E.D., Saraceno, M., 2013. Multiple jets in the Malvinas current. J. Geophys. Res.: Oceans 118 (4), 2107–2117. https://doi.org/10.1002/jgrc.20170.
Piola, A.R., Gordon, A.L., 1989. Intermediate waters in the southwest South Atlantic. Deep sea research Part A. Oceanographic Research Papers 36 (1), 1–16. https://doi.org/10.1016/0198-0149(89)90015-0.
Piola, A.R., Martínez Avellaneda, N., Guerrero, R.A., Jardón, F.P., Palma, E.D., Romero, S.I., 2010. Malvinas-slope water intrusions on the northern Patagonia continental shelf. Ocean Sci. 6 (1), 345–359. https://doi.org/10.5194/os-6-345-2010.
Piola, A.R., Matano, R.P., Palma, E.D., Möller, O.O., Campos, E.J.D., 2005. The influence of the Plata River discharge on the western South Atlantic shelf. Geophys. Res. Lett. 32 (1) https://doi.org/10.1029/2004GL021638.
Piola, A.R., Möller, O.O., Guerrero, R.A., Campos, E.J.D., 2008a. Variability of the subtropical shelf front off eastern South America: winter 2003 and summer 2004. Continent. Shelf Res. 28 (13), 1639–1648. https://doi.org/10.1016/j.csr.2008.03.013.
Piola, A.R., Romero, S.I., Zajaczkovskiab, U., 2008b. Space-time variability of the Plata plume inferred from ocean color. Continent. Shelf Res. 28, 1556–1567. https://doi.org/10.1016/j.csr.2007.02.013.
Provost, C., Escoffier, C., Maamaatuaiahutapu, K., Kartavtseff, A., Garçon, V., 1999. Subtropical mode waters in the south Atlantic Ocean. J. Geophys. Res.: Oceans 104 (C9), 21033–21049. https://doi.org/10.1029/1999JC900049.
Provost, C., Gana, S., Garçon, V., Maamaatuaiahutapu, K., England, M., 1995. Hydrographic conditions in the Brazil-Malvinas Confluence during austral summer 1990. J. Geophys. Res.: Oceans 100 (C6), 10655–10678. https://doi.org/10.1029/94JC02864.
Provost, C., Le Traon, P.-Y., 1993. Spatial and temporal scales in altimetric variability in the Brazil-Malvinas current confluence region: dominance of the semiannual period and large spatial scales. J. Geophys. Res.: Oceans 98 (C10), 18037–18051. https://doi.org/10.1029/93JC00693.
Pujol, M.-I., Faugère, Y., Taburet, G., Dupuy, S., Pelloquin, C., Ablain, M., Picot, N., 2016. DUACS DT2014: The new multi-mission altimeter data set reprocessed over 20 years. Ocean Sci. 12 (5), 1067–1090. https://doi.org/10.5194/os-12-1067-2016.
Reid, J.L., Nowlin, W.D., Patzert, W.C., 1977. On the characteristics and circulation of the southwestern Atlantic Ocean. J. Phys. Oceanogr. 7, 62–91. https://doi.org/10.1175/1520-0485(1977)007<0062:OTCACO>2.0.CO;2.
Roden, G.I., 1986. Thermohaline fronts and baroclinic flow in the Argentine Basin during the austral spring of 1984. J. Geophys. Res. 91 (C4), 5075–5093. https://doi.org/10.1029/JC091iC04p05075.
Rodrigues, R.R., Wimbush, M., Watts, D.R., Rothstein, L.M., Ollitrault, M., 2010. South Atlantic mass transports obtained from subsurface float and hydrographic data. J. Mar. Res. 68 (6), 819–850. https://doi.org/10.1357/002224010796673858.
Romero, S.I., Piola, A.R., Charo, M., Garcia, C.A.E., 2006. Chlorophyll-a variability off Patagonia based on SeaWiFS data. J. Geophys. Res.: Oceans 111 (C5). https://doi.org/10.1029/2005JC003244.
Rühs, S., Schwarzkopf, F.U., Speich, S., Biastoch, A., 2019. Cold vs. warm water route – sources for the upper limb of the Atlantic Meridional Overturning Circulation revisited in a high-resolution ocean model. Ocean Sci. 15 (3), 489–512. https://doi.org/10.5194/os-15-489-2019.
Saraceno, M., Provost, C., 2012. On eddy polarity distribution in the southwestern Atlantic. Deep Sea Res. Oceanogr. Res. Pap. 69, 62–69. https://doi.org/10.1016/j.dsr.2012.07.005.
Saraceno, M., Provost, C., Piola, A.R., 2005. On the relationship between satellite-retrieved surface temperature fronts and chlorophyll a in the western South Atlantic. J. Geophys. Res.: Oceans 110 (C11). https://doi.org/10.1029/2004JC002736.
Saraceno, M., Provost, C., Piola, A.R., Bava, J., Gagliardini, A., 2004. Brazil Malvinas Frontal System as seen from 9 years of advanced very high resolution radiometer data. J. Geophys. Res.: Oceans 109 (C5). https://doi.org/10.1029/2003JC002127.
Sato, O.T., Polito, P.S., 2014. Observation of South Atlantic subtropical mode waters with Argo profiling float data. J. Geophys. Res.: Oceans 119, 2860–2881. https://doi.org/10.1002/2013JC009438.
Schmid, C., Garzoli, S.L., 2009. New observations of the spreading and variability of the antarctic intermediate water in the atlantic. J. Mar. Res. 67 (6), 815–843. https://doi.org/10.1357/002224009792006151.
Schmid, C., Siedler, G., Zenk, W., 2000. Dynamics of intermediate water circulation in the subtropical South Atlantic. J. Phys. Oceanogr. 30 (12), 3191–3211. https://doi.org/10.1175/1520-0485(2000)030<3191:DOIWCI>2.0.CO;2.
Simionato, C.G., Nuñez, M.N., Engel, M., 2001. The salinity front of the Río de la Plata: A numerical case study for winter and summer conditions. Geophys. Res. Lett. 28, 2641–2644. https://doi.org/10.1029/2000GL012478.
Sloyan, B.M., Rintoul, S.R., 2001. Circulation, renewal, and modification of antarctic mode and intermediate water. J. Phys. Oceanogr. 31, 1005–1030. https://doi.org/10.1175/1520-0485(2001)031<1005:CRAMOA>2.0.CO;2.
Sloyan, B.M., Talley, L.D., Chereskin, T.K., Fine, R., Holte, J., 2010. Antarctic intermediate water and subantarctic mode water formation in the southeast pacific: the role of turbulent mixing. J. Phys. Oceanogr. 40 (7), 1558–1574. https://doi.org/10.1175/2010JPO4114.1.
Spadone, A., Provost, C., 2009. Variations in the Malvinas current volume transport since october 1992. J. Geophys. Res.: Oceans 114 (C2). https://doi.org/10.1029/2008JC004882.
Stramma, L., Peterson, R.G., 1990. the South atlantic current. J. Phys. Oceanogr. 20 (6), 846–859. https://doi.org/10.1175/15200485(1990)020<0846:Tsac>2.0.Co;2.

Strub, P.T., James, C., Combes, V., Matano, R.P., Piola, A.R., Palma, E.D., Saraceno, M., Guerrero, R.A., Fennco, H., Ruiz-Etcheverry, L.A., 2015. Altimeter-derived seasonal circulation on the southwest Atlantic shelf: 27°–43°S. J. Geophys. Res.: Oceans 120 (5), 3391–3418. https://doi.org/10.1002/2015JC010769.

Talley, L.D., 1996. Antarctic intermediate water in the south atlantic. In: The South Atlantic. Springer, Berlin, Heidelberg. https://doi.org/10.1007/978-3-642-80353-6_11.

Tsuchiya, M., Talley, L.D., McCartney, M.S., 1994. Water-mass distributions in the western South Atlantic; A section from South Georgia Island (54S) northward across the equator. J. Mar. Res. 52 (1), 55–81. https://doi.org/10.1357/0022240943076759.

Valla, D., Piola, A.R., 2015. Evidence of upwelling events at the northern Patagonian shelf break. J. Geophys. Res.: Oceans 120 (11), 7635–7656. https://doi.org/10.1002/2015JC011002.

Valla, D., Piola, A.R., Meinen, C.S., Campos, E., 2018. Strong mixing and recirculation in the northwestern Argentine Basin. J. Geophys. Res.: Oceans 123, 4624–4648. https://doi.org/10.1029/2018JC013907.

Vigan, X., Provost, C., Bleck, R., Courtier, P., 2000. Sea surface velocities from sea surface temperature image sequences: 1. Method and validation using primitive equation model output. J. Geophys. Res.: Oceans 105 (C8), 19499–19514. https://doi.org/10.1029/2000JC900027.

Vivier, F., Provost, C., 1999a. Direct velocity measurements in the Malvinas Current. J. Geophys. Res.: Oceans 104 (C9), 21083–21103. https://doi.org/10.1029/1999JC900163.

Vivier, F., Provost, C., 1999b. Volume transport of the Malvinas Current: can the flow be monitored by TOPEX/POSEIDON? J. Geophys. Res.: Oceans 104 (C9), 21105–21122. https://doi.org/10.1029/1999JC900056.

Wainer, I., Gent, P., Goni, G., 2000. Annual cycle of the Brazil-Malvinas confluence region in the national center for atmospheric research climate system model. J. Geophys. Res.: Oceans 105 (C11), 26167–26177. https://doi.org/10.1029/1999JC000134.

Worthington, L.V., 1976. On The north atlantic circulation. In: Johns Hopkins Oceanographic Studies, vol. 6. John Hopkins University Press, Baltimore, Md, p. 110.

You, Y., 2002. Quantitative estimate of antarctic intermediate water contributions from the Drake passage and the southwest Indian ocean to the south atlantic. J. Geophys. Res.: Oceans 107 (C4). https://doi.org/10.1029/2001JC000880, 6-1-6-20.

Zweng, M.M., Reagan, J.R., Antonov, J.I., Locarnini, R.A., Mishonov, A.V., Boyer, T.P., Garcia, H.E., Baranova, O.K., Johnson, D.R., Seidov, D., Biddle, M.M., 2013. world ocean Atlas 2013, volume 2: salinity. In: Levitus, S., Mishonov Technical, A. (Eds.), NOAA Atlas NESDIS, vol. 74, p. 39.